A Regularization Technique for the Analysis of Photographic Data Used in Chemical Release Wind Measurements

---

A Thesis
Presented to
the Graduate School of
Clemson University

In Partial Fulfillment
of the Requirements for the Degree
Master of Science
Electrical Engineering

---

by
Justin Edward Ingersoll
August 2008

Accepted by:
Dr. Stanley Birchfield, Committee Chair
Dr. Miguel Larsen
Dr. Timothy Burg

Abstract

The neutral winds are a key parameter in the electrodynamics of the ionosphere. The available techniques for measuring vertical neutral wind profiles, especially with good height resolution, are extremely limited. This is especially true with sounding rocket flights as it is not practical to take direct measurements of neutral winds with onboard instruments. Chemical releases from sounding rockets, however, allow such measurements by providing a tracer of the motion of the neutral atmosphere at altitudes in the mesosphere and lower thermosphere (MLT). The resulting chemiluminescent trail is typically photographed from two or more locations to track neutral motions. Triangulation based on these photographs then yields position information at each instant when simultaneous photographs are available from different locations. The resulting time series of position information can then be used to obtain a neutral wind profile. A technique is presented that improves this existing triangulation procedure by implementing computer vision-based automation techniques and an improved tracking algorithm that can accommodate non-simultaneous image data more easily and can provide better continuity in the motions inferred from consecutive images. Neutral wind profiles from the Joule II and HEX II sounding rocket experiments are presented and compared with results from the previous method.

Dedication

To my parents and sister. Thank you.

Acknowledgments

I would like to thank Dr. Miguel Larsen for being my advisor in physics and for supporting my research. I would also like to thank Dr. Stanley Birchfield for being my advisor in electrical and computer engineering and Dr. Timothy Burg for serving on my committee. Dr. Larsen and Dr. Birchfield both contributed significantly to the success of my research and the ideas behind my algorithms.

Patti Larsen deserves special mention for her support and all the effort she puts in behind the scenes to keep things running smoothly and keep us all organized. I would also like to acknowledge the staff of the Physics Machine Shop – Lamar Durham, Brian Turpin, and Jonathan Simpson – for their help and ideas during my development of the new camera system used to collect the data used in this thesis.

Table of Contents

List of Tables

List of Figures

Chapter 1

Introduction

This thesis is an interdisciplinary project with collaboration between both physics and electrical and computer engineering. Image and signal processing techniques from engineering are used to enhance and partially automate a data analysis task from atmospheric physics.

1.1 Science Overview

An overview of the science and structure of the neutral atmosphere and ionosphere of the earth is provided to give an appropriate background for the physics motivating this project.

1.1.1 Neutral Atmosphere

The neutral atmosphere of the earth consists of several layers, most notably the troposphere, stratosphere, mesosphere, and thermosphere. These layers and their respective temperatures are depicted in Figure 1.1. The troposphere is the lowest layer of the atmosphere and ranges from the ground to tropopause, located at 12 km.

Temperatures decrease with altitude due to adiabatic cooling (a rising parcel of air expands, and must therefore cool due to conservation of energy). The stratosphere ranges from the tropopause to the stratopause at 45 km. Ozone in this layer absorbs ultraviolet light from the sun, resulting in a temperature increase with altitude since ozone density also increases with altitude. Atmospheric temperature reaches a local maximum at the stratopause which separates the stratosphere from the mesosphere. Temperature decreases through the mesosphere due to radiation of infrared energy to space by various chemical constituents. Finally, temperatures again begin to increase starting at the mesopause (85 km) due to extreme ultraviolet (EUV) absorption by oxygen. The T on the temperature plot in Figure 1.1 represents the turbopause, where turbulent mixing gives way to molecular diffusion. For more details, see[7].

1.1.2 Ionosphere

The earth's ionosphere consists of layers of ionized gas located in the mesosphere and thermosphere. This ionization is caused by absorption of solar radiation in the regions that are sunlit. The most significant layers occur at 60-90 km, 90-180 km, and 180-1500 km, known, respectively, as the D, E, and F layers. Figure 1.1 illustrate these layers and their respective electron densities. During the day, the F layer splits into the F1 and F2 layers. As the sun sets, the D layer disappears almost immediately because the atmosphere is dense enough that recombination occurs very quickly. The E layer recombines more gradually as the atmosphere is much less dense at E-region altitudes, which translates into a longer mean free path and lower collision frequencies. Finally, the F1 and F2 layers merge into a single F layer and remain throughout the night. See Houton [7] and Zhan [22] for more detail.

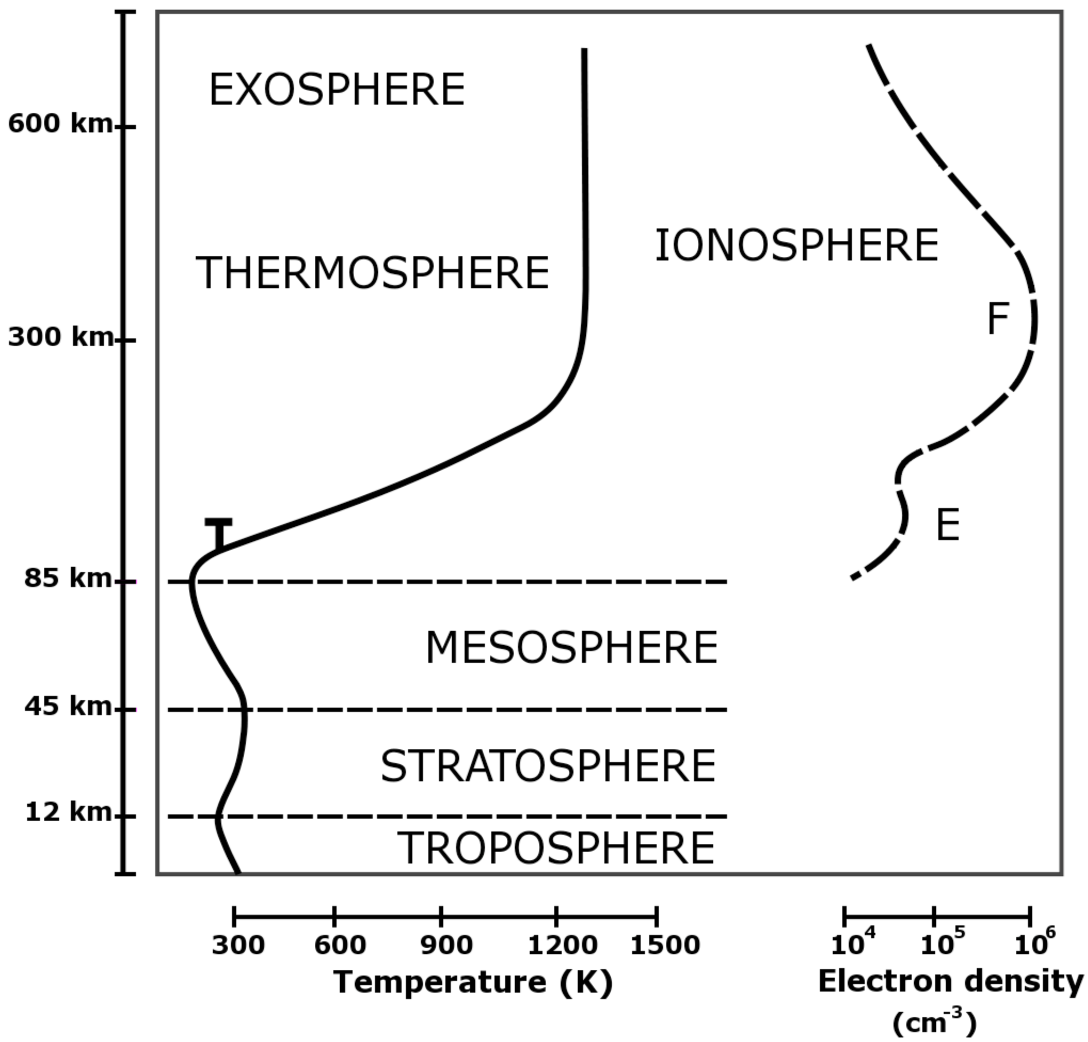

Figure 1.1: Layers of the Atmosphere and Ionosphere (Image is Public Domain)

The neutral winds are an important parameter in nearly all ionospheric processes. In the context of atmospheric physics, neutral winds are the movement of the uncharged components of the atmosphere, while the movements of charged particles are referred to as plasma drifts. The winds are particularly important in the electrodynamics of the ionosphere as the electric fields of interest are those in the frame of the neutrals. In other words, the reference frame for the electric fields is tied to the movement of the neutral particles rather than the stationary background atmosphere. This is especially true at low and mid latitudes where the neutral velocities and plasma drifts are of similar magnitude. As density in the atmosphere increases, ions transition from drifting in ($\boldsymbol{E} \times \boldsymbol{B}$) direction, the so-called magnetized state, to being dragged along with the neutrals, the so-called collisional state. In other words, the ions become collisional in the MLT region and plasma drift velocities should be comparable to neutral wind velocities. [10]

1.2 Motivation

As described above, knowledge of the movement of the neutral components of the atmosphere is a key component of any study of the ionosphere. This is especially true with sounding rocket flights as it is not practical to take direct measurements of neutral winds with onboard instruments. Ground-based instruments, such as Doppler lidars, Fabry-Perot interferometers, and incoherent scatter radars, can be used to remotely measure neutral winds, but they either require assumptions that are sometimes questionable or have limited altitude coverage. As rockets provide small-scale, in-situ measurements of ionospheric parameters, in-situ wind measurements in the vicinity of the rocket trajectory are desirable. Chemical releases from sounding rockets provide this capability. Typical chemical payloads include barium, sodium, potassium, and trimethyl aluminum (TMA). This thesis focuses on TMA releases and the determination of neutral winds from them.

1.3 Experiment Overview

TMA is a pyrophoric compound that reacts on contact with oxygen to produce chemiluminescence. At ground level, this reaction is very rapid and results in flame. At high altitudes, the oxygen density is much lower, which results in much slower reaction rates. This permits released TMA clouds to remain visible to the naked eye – and to cameras – for at least five minutes and, depending on conditions, for thirty minutes or longer. As the TMA and the products of its reaction with oxygen are neutral and do not ionize, it is suited to measuring the movement of the neutral atmosphere.

Rocket trajectories for TMA releases are fairly low, with apogees typically on the order of 200 kilometers. This puts the rocket at E region altitudes during a significant fraction of the flight. TMA is typically released during the upleg and downleg phases of the flight. The *upleg* refers to the ascent of the rocket prior to apogee while the *downleg* occurs after apogee when the rocket is descending. Releases normally take place between approximately 80 and 180 kilometers. As the rocket trajectory, and hence the initial distribution of the TMA is known, subsequent deformations of the trail are a result of the neutral winds. In addition, the gas is not released in a constant stream, but rather is puffed to produce discrete clouds. These clouds permit easier identification of corresponding points in photographs taken from different locations.

As the TMA release takes place, it is observed from several widely-spaced ground locations. The events are photographically recorded for offline processing. Cameras typically include 35 mm film and digital SLRs, 70 mm medium-format Hasselblads, and low-light, intensified CCD video recorders. At least two and ideally three or more camera sites are used to provide several triangulation baselines.

1.4 Analysis Overview

The overall goal of the analysis is to determine the neutral winds from photographs of TMA releases. In the past, analysis of the images and wind profile generation was done with a user-input intensive port of legacy FORTRAN code. It is desired to update and modernize both the procedure and the wind-determination algorithm itself. Instead of merely determining the location of the TMA trail at several times and, from that, calculating the corresponding wind, a regularization algorithm that does not depend on simultaneous images is used.

Chapter 2 describes the image processing and computer vision techniques used to process the images of TMA trails to isolate the starfield located in the background of the image as well as the TMA present in the foreground. The starfield information can then be used to calculate plate constants, which are used to precisely determine the location of the image in the sky. The TMA points are used in the automated triangulation and regularization procedures.

Chapter 3 describes the traditional and improved triangulation algorithms used to seed the regularization procedure. The triangulation algorithm is based on multiple pairs of simultaneous or near-simultaneous images from two different camera sites. The traditional implementation is fairly opaque and difficult to follow. The improved version, however, automatically solves for vectors to TMA clouds and their position explicitly.

Chapter 4 presents the tracking and regularization wind determination procedures. The tracking algorithm uses the traditional triangulation algorithm with simultaneous images to determine an estimate of the wind velocity and initial position. These initial conditions are determined using the above-described automated triangulation procedure [14]. A genetic algorithm-based search over the four-dimensional solution space at each altitude is then used to determine the most likely wind and position profiles.

Chapter 5 gives two real-world applications of the entire wind determination procedure. A downleg release from the Joule II sounding rocket experiment and an upleg release from the HEX II sounding rocket experiment are processed. Chapter 6 includes discussion and conclusions based on these results. Appendix A details the date and time systems used, while Appendix B covers coordinate systems. Appendix C enumerates the coordinate system conversions relevant to the triangulation and wind determination procedures. Finally, Appendix D contains a derivation of the closest approach of two vectors used in the triangulation procedures.

1.5 Related Works

Many TMA releases have been conducted over the last 50 years. Several researchers have developed methods for determining neutral winds from photographs of the releases. The most notable of these include Miguel Larsen [13] at Clemson University and Eugene Wescott [21] at the Geophysical Institute, University of Alaska, Fairbanks. The Larsen technique is described and referenced throughout this thesis as the traditional triangulation method. The Wescott technique, however, is similar in concept to the regularization technique presented in this thesis, but is more limited in altitude range and is not automated.

Chapter 2

Image Processing

2.1 Source Images

Three different types of cameras are used to photograph the TMA trails. The primary camera system consists of Nikon Digital SLR cameras – currently D70 and D80 models. The backup system uses medium-format Hasselblad film cameras. Finally, film Nikon SLR cameras and CCD video cameras were used for some experiments, but have since been replaced by digital cameras for future launches.

Figure 2.1 shows a typical image of a TMA trail taken with a digital SLR camera – a Nikon D80 with a 35 mm, f/1.4 lens (effective focal length: 52.5mm due to sensor size). This image includes all of the features that are commonly found in TMA trail photographs: TMA trails, auroral arcs, and background stars. Taken on January 19, 2007 at 12:32:51 UT from the Poker Flat Research Range, this image is from the Joule II experiment.

The trail is seen to spiral around a central point because it is an upleg photographed from the launch site. The resultant image looks directly up the trail, parallel to the

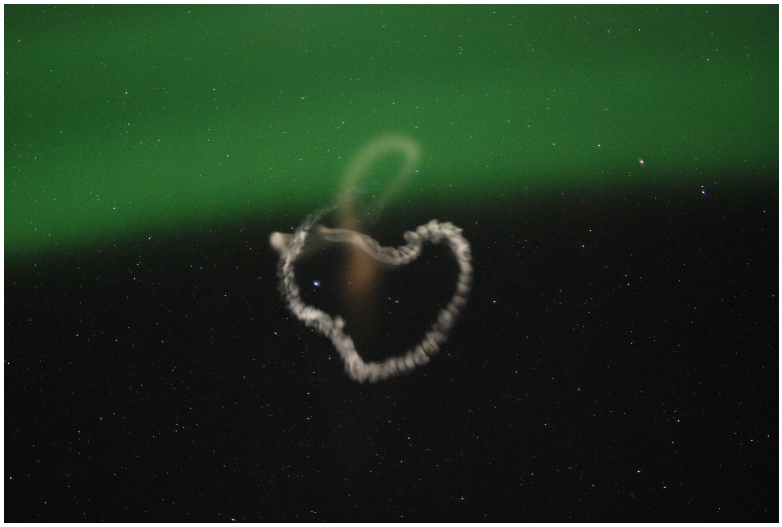

Figure 2.1: Representative Digital SLR Image - Upleg TMA Release from Poker Flat, AK (19 January 2007, 12:32:51 UT)

rocket's motion. The trail itself consists of two different regions. The lower region is white in color and somewhat resembles a dashed line. The dashed pattern is caused by releasing the TMA in discrete puffs rather than a continuous flow. The white color indicates that the trail is in a portion of the atmosphere below the turbopause – the boundary between the homosphere and heterosphere. Turbulent mixing dominates in the homosphere, while molecular diffusion dominates in the heterosphere [18]. The upper region of TMA trail becomes smooth and yellow-orange in color above the turbopause.

Also in the image is a discrete auroral arc, spanning the upper third of the image. The green color is due to the 557.7 nm atomic oxygen emission. The auroral arc in this image is fairly bright, partially washing out the TMA trail and starfield behind it. Images from other times and places will have differing auroral displays in the background, depending on the auroral event and time of year. Of course, images taken outside of the polar regions will contain no aurora at all.

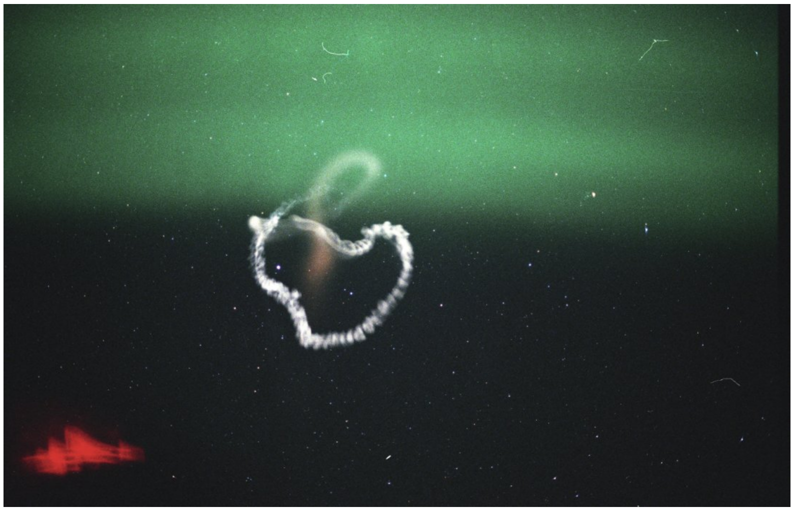

Figure 2.2: Representative Nikon Film SLR Image - Upleg TMA Release from Poker Flat, AK (19 January 2007, 12:32:50 UT)

The image also contains a background starfield. The constellation Ursa Minor spans the right two thirds of the image and the brightest star in the image, Polaris, is located in the left side of the TMA loop. Recognizable stars are important as they allow the calculation of the exact part of the sky in the image. The stars are not simply circles, with size corresponding to brightness. Rather, since the image was taken with a digital camera utilizing a CCD, the pixels around brighter stars bloom. Bloom refers to the overflow of a pixel in a CCD to the surrounding pixels that occurs when too bright an object is imaged. It is an indication that the feature in question is overexposed.

In addition to the Nikon digital cameras, Nikon film cameras are used. Figure 2.2 was captured using a Nikon F3 camera with a 50 mm, f/1.2 lens and high speed film. The photograph was taken one second earlier than the digital image in Figure 2.1 and captures the same event. In addition to the TMA trail, stars, and auroral arc described above, this image includes a red timestamp in the lower left corner. Ideally, there would be 6 digits showing the time (hours, minutes, and seconds), but it did not come out properly in this image, leaving a red blur.

The third and final camera type used is the medium-format Hasselblad EL/M 500 (and the corresponding 80 mm, f/2.8 lens). Typically, high speed film and long exposures are used to ensure that sufficient stars are visible. Unlike the first two cameras, black and white film (3200 speed Kodak TMAX) is used in the Hasselblad cameras, making it somewhat more difficult to differentiate faint TMA trails from background aurora. Figure 2.3 shows the same event as the other two cameras, but is a 20-second exposure (significantly longer than the 5 second exposures of the digital and film SLRs). As in the Nikon film image, this image has a timestamp in the lower left corner. In this case, the number 12 is visible (image is reversed), but the rest of the time display is washed out. Due to the high speed of the film and push processing used, images from the Hasselblad cameras show an excessive amount of film grain (essentially noise). To combat this, Hasselblad images are smoothed by convolution with a 3-by-3 Gaussian kernel prior to processing. This smoothing process does not significantly affect the brightness or position of stars in the image as they are larger than the convolution kernel used.

2.2 Determination of Plate Constants

The first step in processing a set of images is to determine the plate constants for each image. Knowledge of the plate constants of an image is required before any other calculations are possible. Plate constants are the parameters of the linear transformation from plate coordinates (physical measurements on the negative or sensor) to astronomical or standard coordinates. A MATLAB GUI implementing the

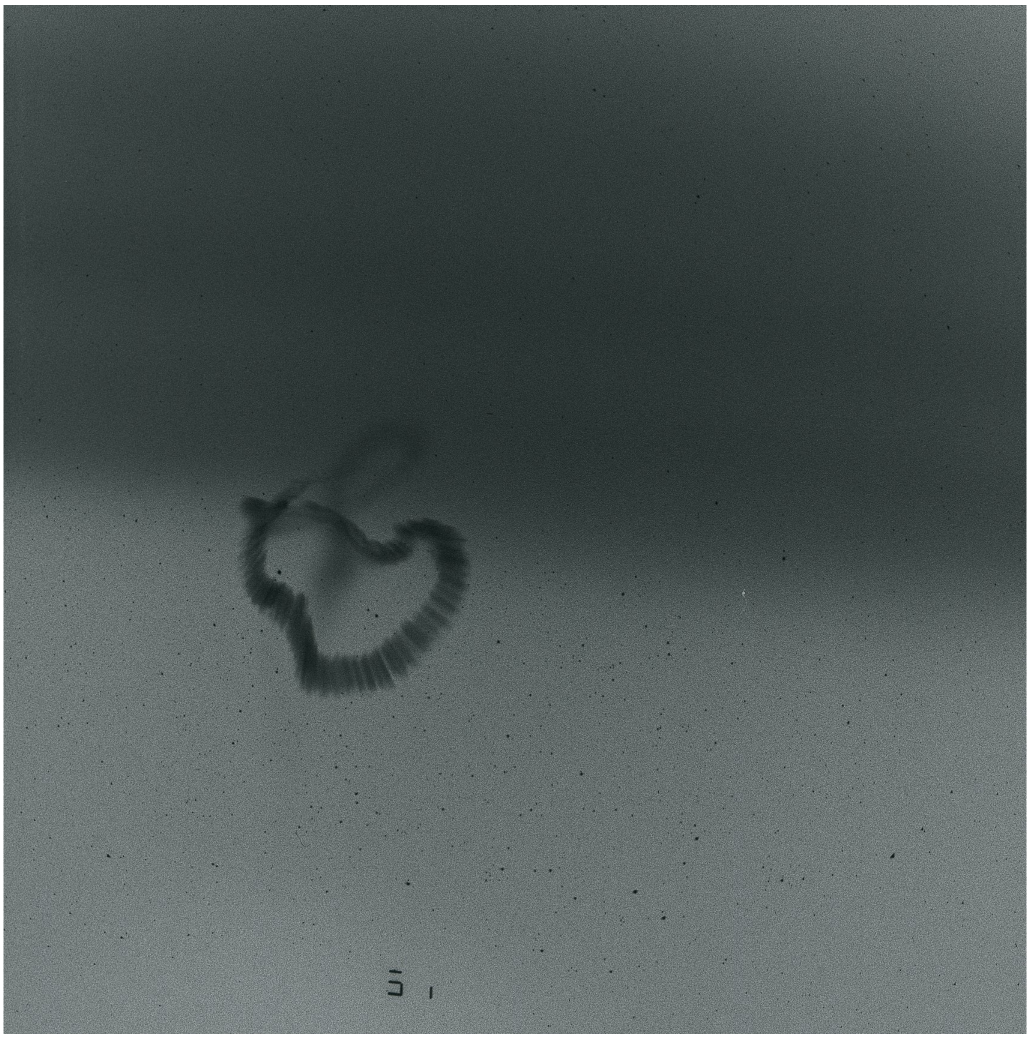

Figure 2.3: Representative Hasselblad Image - Upleg TMA Release from Poker Flat, AK (19 January 2007, 12:32:40 UT)

following algorithm and procedures has been written.

If the instrument that captured the image was precisely aligned to the axes of the standard coordinate system, the transformation from plate (x, y) to standard coordinates (X, Y) would be a simple projection based on the focal length F of the lens used: i.e. $X = \frac{x}{F}$ and $Y = \frac{y}{F}$. If the coordinates of the exact center of the image were also known, the standard coordinates could then be transformed to astronomical equatorial coordinates (α, δ), i.e, right ascension and declination. [1]

The conditions that allow the use of the simple projection are almost always not met as the precise camera pointing is not known. A general linear transformation given by

$$
\begin{aligned}
X &= ax + by + c \\
Y &= dx + ey + f
\end{aligned}
\tag{2.1}
$$

is used in place of the simple projection. Here a, b, c, d, e, and f are the plate constants for an image. They completely specify the affine transformation (2.1) from plate coordinates to standard coordinates.

2.2.1 Identification of Background Stars

Prior to actually calculating the plate constants, the background stars in the image must be located and identified. Given the nature of the photos with bright star points set against a darker background, simple filtering techniques can be utilized to isolate the stars. Small bright points against a dark background are high-frequency features, so a high-pass filter is suitable for isolating them from the lower frequency background.

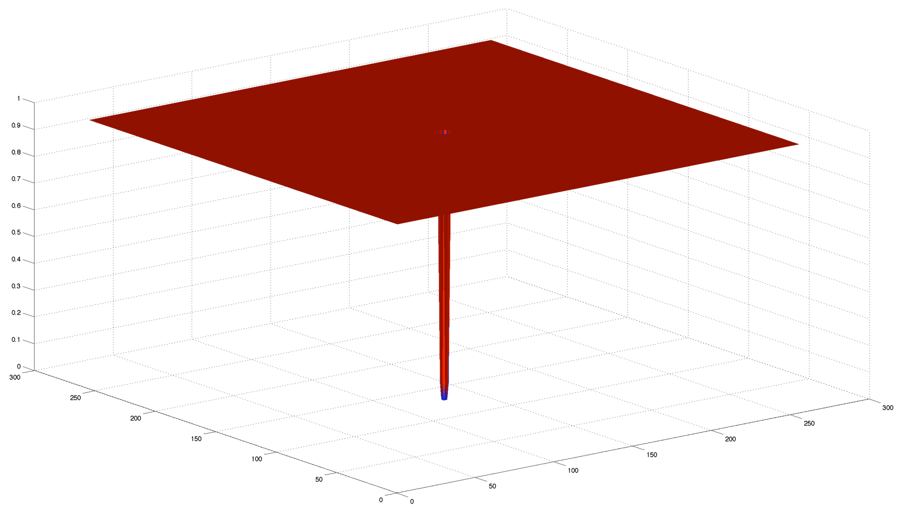

Figure 2.4: Frequency Domain High Pass Filter

A frequency-domain high-pass Butterworth filter, depicted in Figure 2.4, is used to separate background stars from the rest of the image. This specific filter uses a normalized cutoff frequency of 0.01 (normalized range is from 0 to 1) [12]. The filter is applied in the frequency domain by taking the two-dimensional Fourier transform of the image to be filtered, multiplying by the filter, and then taking the inverse two-dimensional Fourier transform. The result of applying this filtering process to Figure 2.1 is illustrated in Figure 2.5. Typically, a window function that is one-valued over most of the image but tails off to zero at the edges would first be multiplied onto the image prior taking to the Fourier transform. This is used to suppress the artificial high-frequency features that exist at the edges of an image when a bright feature essentially transitions immediately to zero where the image ends. A window function is not used here because the images in general tail off to zero at the edges already. [6]

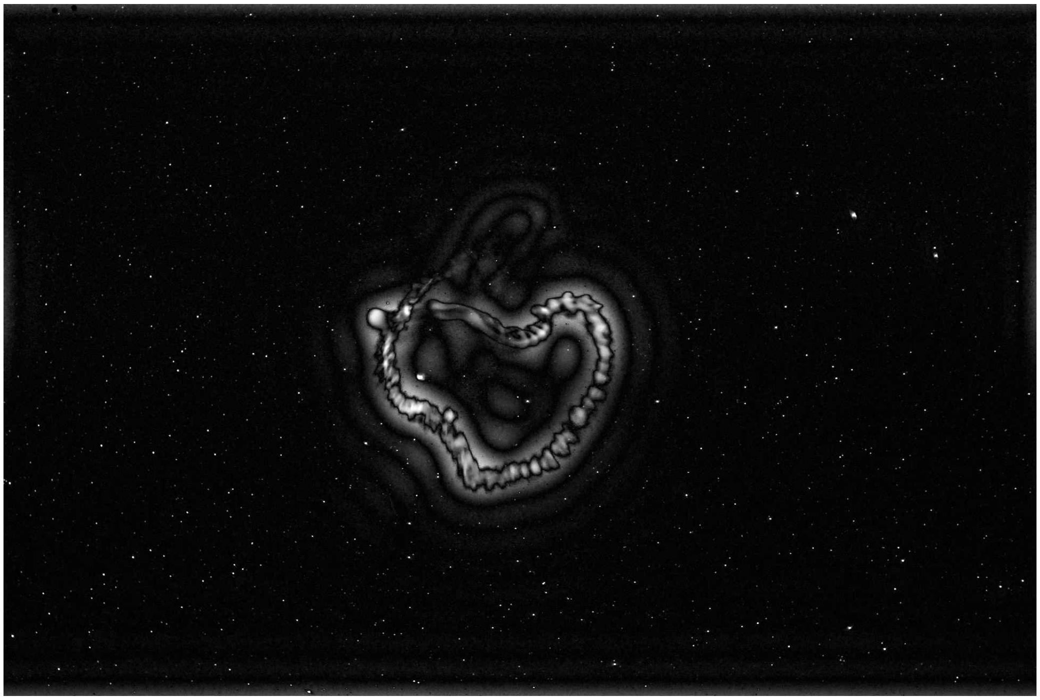

Figure 2.5: Application of High-Pass Filter to Figure 2.1

Prior to filtering, color images are converted to grayscale by discarding the green channel and averaging the red and blue channels. This, along with the filtering process, eliminates the aurora and any other low frequency components of input image. However, the filtering process has introduced ringing around the TMA trail and the edges of the image due to the steepness of the filter used. The stars present in the image have been isolated, but the the high-frequency components of the TMA trail are also present. Edges of the TMA trail are high-frequency features because they produce a sharp transition from the dark background to the bright foreground. Three further steps are used to produce an image which only contains stars: histogram equalization, thresholding, and area-based culling. Immediately following the filtering operation, depending on the type of image, some areas are zeroed out to remove edge effects and the timestamp from the image. Figure 2.6a illustrates this procedure.

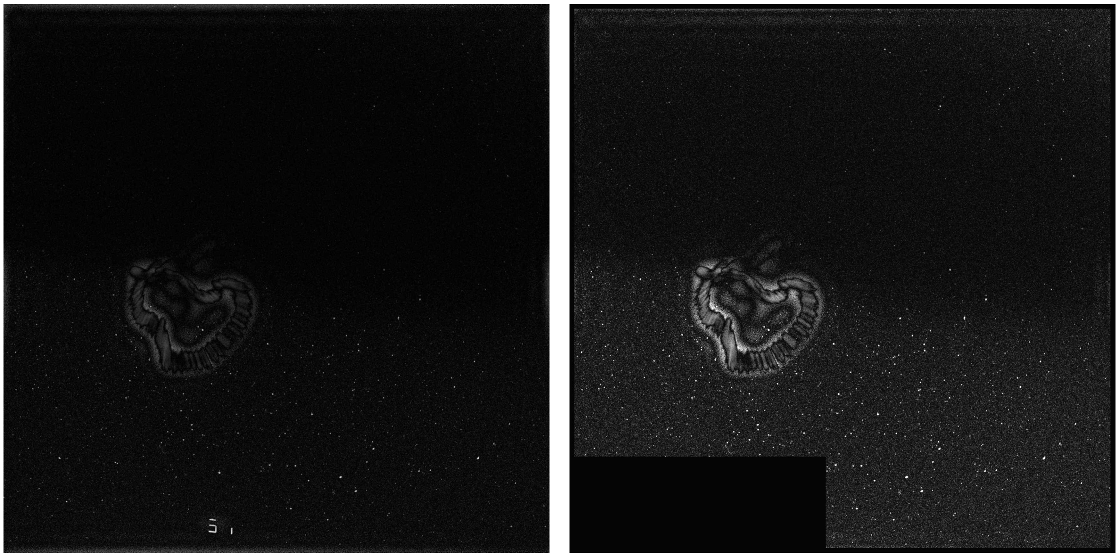

(a) (b)

Figure 2.6: (a): Result of applying high-pass filter to Hasselblad sample image (Figure 2.3). (b): Figure 2.6a after applying histogram equalization

Histogram equalization is then used to enhance the contrast in the filtered images. In some cases, the image may not take up the full dynamic range available in an eight-bit grayscale image (256 levels). An image histogram is a tool which plots the number of pixels at each possible intensity. It allows the identification of unused gray levels. In this case, gray levels with zero pixels present at the white end of the histogram are eliminated and the image is resampled in intensity to fill the entire grayscale spectrum. The result of this operation is illustrated in Figure 2.6b.

The final steps in separating the stars from the rest of the image are the thresholding and culling operations. Thresholding is an operation that converts a grayscale image to a binary image. All gray values below the threshold are set to zero and all gray values greater than or equal to the threshold are set to one. The default threshold is 150, but the optimal value is highly sensitive to variations in image brightness

(a)

(b)

Figure 2.7: Result of applying complete star detection process to Figure 2.1 with threshold values of (a) 150 and (b) 200

and background aurora. Manual tuning of the threshold value is possible to find this optimal value. After thresholding, stars and other objects that are too dim to be useful stars have been discarded, but bright, non-star regions may remain. A culling operation is performed to eliminate these regions by setting the maximum number of pixels a star can occupy to 150. Any region larger than the maximum is set to zero to remove it from consideration. At this point, the only remaining regions represent stars. Since the regions are not necessarily regular, the actual coordinates of the stars are determined from the centroids of the remaining regions.

Figure 2.7 illustrates the results of the complete star-detection algorithm. Detected stars are marked with yellow asterisks. Note that Figure 2.7b shows an approximately ideal density of detected starts, while Figure 2.7a has far too many stars (resulting from too low of a threshold). In some circumstances particularly bright areas in the aurora or TMA trail may be detected as stars, so an additional manual culling step is also available if needed.

2.2.2 Preliminary Solution

At this point the image has been preprocessed, yielding a list of pixel coordinates of detected stars. This is half of the information needed to solve for the plate constants. The other set of information is the standard coordinates of a set of corresponding actual star positions. The Smithsonian Astrophysical Observatory (SAO) Catalog [16] is used as the source of these star coordinates. Only stars of apparent magnitude 5 or brighter, i.e. magnitude ≤ 5 are used since the detection process outlined above is designed to keep only the brightest stars in the image. Apparent magnitude is a measure of the brightness of a star as viewed from Earth. Bright stars have small or negative values while dim stars have large apparent magnitudes.

The SAO Catalog, of course, contains stars much dimmer than magnitude 5, so only a subset of the catalog is used, reducing search times. A simple FORTRAN program is used to process the catalog and output a smaller catalog containing only the desired stars. [6]

One more piece of information is required before the preliminary solution can be calculated: the approximate center of the image. This is required to calculate the conversion from equatorial coordinates from the star catalog to standard coordinates. Appendix B describes the coordinate systems used here. The center can be estimated by comparing the photograph with interactive star catalog software such as Stellarium [2]. From this information, a subset of the magnitude 5 catalog can be determined by selecting the stars within the approximate field of view of the camera's lens, centered on the estimated center point.

The transformation (2.1) has 6 unknown quantities, but only two equations, so a total of three known pairs of detected and catalog stars are required to determine a solution. This results in a system of 6 equations in 6 unknowns, shown in (2.2), which can then be solved for an exact solution. The (X_i, Y_i) pairs are the calculated standard coordinates of a catalog star and (x_i, y_i) are the pixel coordinates of a corresponding detected star.

$$\begin{aligned}
X_1 &= ax_1 + by_1 + c \\
X_2 &= ax_2 + by_2 + c \\
X_3 &= ax_3 + by_3 + c \\
Y_1 &= dx_1 + ey_1 + f \\
Y_2 &= dx_2 + ey_2 + f \\
Y_3 &= dx_3 + ey_3 + f
\end{aligned} \tag{2.2}$$

These three pairs must be obtained from user input as there is not yet enough information to automatically find matched pairs. An interactive plot is used to accomplish this matching. The standard coordinates of the above visible subset of the catalog are plotted. Then the standard coordinates of the detected stars are crudely estimated with the simple perspective projection (2.3) and plotted on the same axes. This projection does not take into account any rotation or scaling caused by the orientation of the camera or nonlinearity of the camera and lens system, respectively. However, the projection is sufficient to allow manual matching of the detected and star patterns and the identification of corresponding stars.

$$
\begin{aligned}
X &= \frac{x}{F} \\
Y &= \frac{y}{F}
\end{aligned}
\tag{2.3}
$$

These three pairs of stars are sufficient to solve the system of equations – (2.2) – for a preliminary set of plate constants. This equation can then automatically be refined to produce a more accurate final set of plate constants.

2.2.3 Refined Solution

A refined solution for the plate constants can now be determined automatically from the above-described user-directed preliminary solution. An overdetermined system of equations using more than 3 pairs of matched stars can be set up and solved with a least-squares estimation. This results in a much more accurate set of plate constants.

In addition to the least squares solution, an iterative approach is used to allow the solution to converge and minimize error. In addition to calculating the plate constants, the precise equatorial and horizontal coordinates of the center of the image are determined.

The preliminary solution allows for a much more precise solution to the standard coordinates of the detected stars as well as a better estimation of the coordinates of the center of the image. An automated matching procedure is used to pair detected and catalog stars. The distance (in standard coordinates) from each detected star to all catalog stars is calculated, and the closest match – conditioned by a maximum

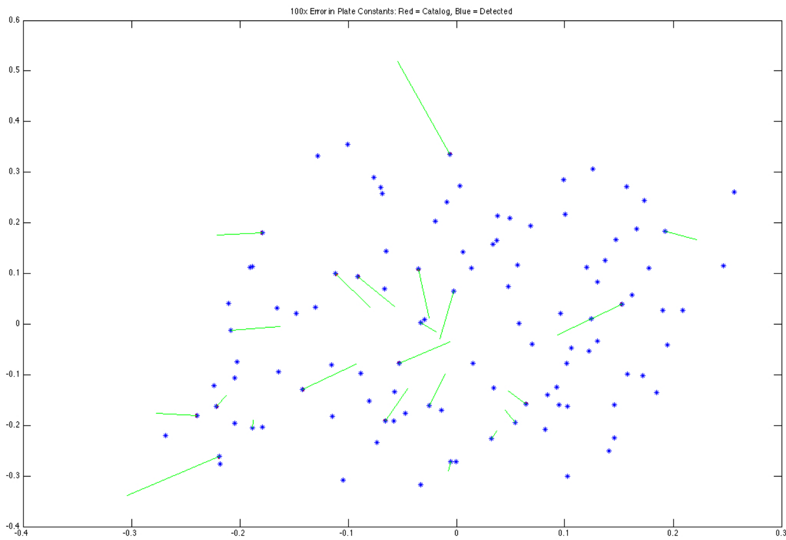

Figure 2.8: Plate Constants Solution Error Plot

allowed distance – is selected. Any cases where multiple detected stars are paired with the same catalog star are eliminated.

This new list of matched stars can then be used to calculate a new set of plate constants using a least-squares error-minimization approach. These new plate constants are then used to recalculate the coordinates of the center of the image.

Next, an iterative approach is used to refine the solution. The newly calculated image center is now used to calculate new standard coordinates for the catalog stars. These new standard coordinates are used to calculate new plate constants and then a new image center. This process is repeated iteratively until the image center coordinates converge. The final plate constants and the center are then saved to a file to allow later processing and are used to generate an error plot.

Figure 2.8 shows a typical error plot, with the visible catalog stars plotted with red dots and the detected stars plotted with blue stars. The green lines represent 100 times the error vectors for each pair of detected and catalog stars. Note that not all detected stars have been matched. Successful calculation of plate constants will result in a plot like this with many matched stars and no definite trend in error vectors (i.e. all toward one direction). Most error plots resemble this plot in that star pairs near the center of the image have error vectors pointing inward, and star pairs near the edge have error vectors pointing outward. This is representative of the distortion inherent in the lens used on the camera.

2.3 Detection of TMA

It is desirable to automatically detect the location of TMA in photographs of trails because manual identification is a time-consuming process, especially considering there are between 3 and 12 photographs per minute per camera per site to be processed for each 5 to 20 minute long TMA trail. On average there are approximately 15 to 25 images per camera site per trail (upleg or downleg). Color images of TMA trails, as depicted in Figures 2.1 and 2.2, show white and rough or smooth and orange regions, depending upon altitude. Black and white images like Figure 2.3, of course, lack color, but show similar rough and smooth regions. The overall goal of TMA detection is a single-pixel-wide trace through the image that follows the center of the trail.

The consistency offered by using an automatic routine to find TMA is important. Rather than relying on user input, which can vary from image to image, the automatic routine will operate on all images in a consistent manner.

One key characteristic present in both color and black and white images is the brightness of the trail versus the background. Some portions of the trail in some images are saturated and have large areas of pure white (gray level 255), while others are only a few tens of gray levels brighter than the background. The resulting large dynamic range in some images makes simple thresholding to identify regions of TMA difficult at best. A more sophisticated approach is required. Both watershed segmentation and the snakes algorithm were investigated as possible solutions to this problem, as explained below.

Identification of regions containing TMA is one of a class of problems in image processing and computer vision known as segmentation. Informally, segmentation consists of carving an image into disjoint regions corresponding to different objects.

One useful tool in this situation is watershed segmentation. [19] Watershed segmentation envisions a grayscale image as a topological map and finds watersheds. A watershed in the geological sense is a region in which all deposited precipitation ends up in the same location. For example, the Rocky Mountains divide the United States into two watersheds, one leading to the Pacific Ocean, and the other leading to the Atlantic. A similar concept can be applied to images as a method of segmenting. Water is flooded up from holes poked in an image and watersheds are determined from a bottom-up approach with each watershed representing a segment in the original image. Watershed segmentation is typically performed on the gradient magnitude of an image because sharp transitions in gray level tend to indicate distinct objects. Figure 2.9 illustrates the application of watershed segmentation to two different photos of TMA trails. The colored regions represent different watersheds and therefore different segments of the image. The images are oversegmented and some trail features are

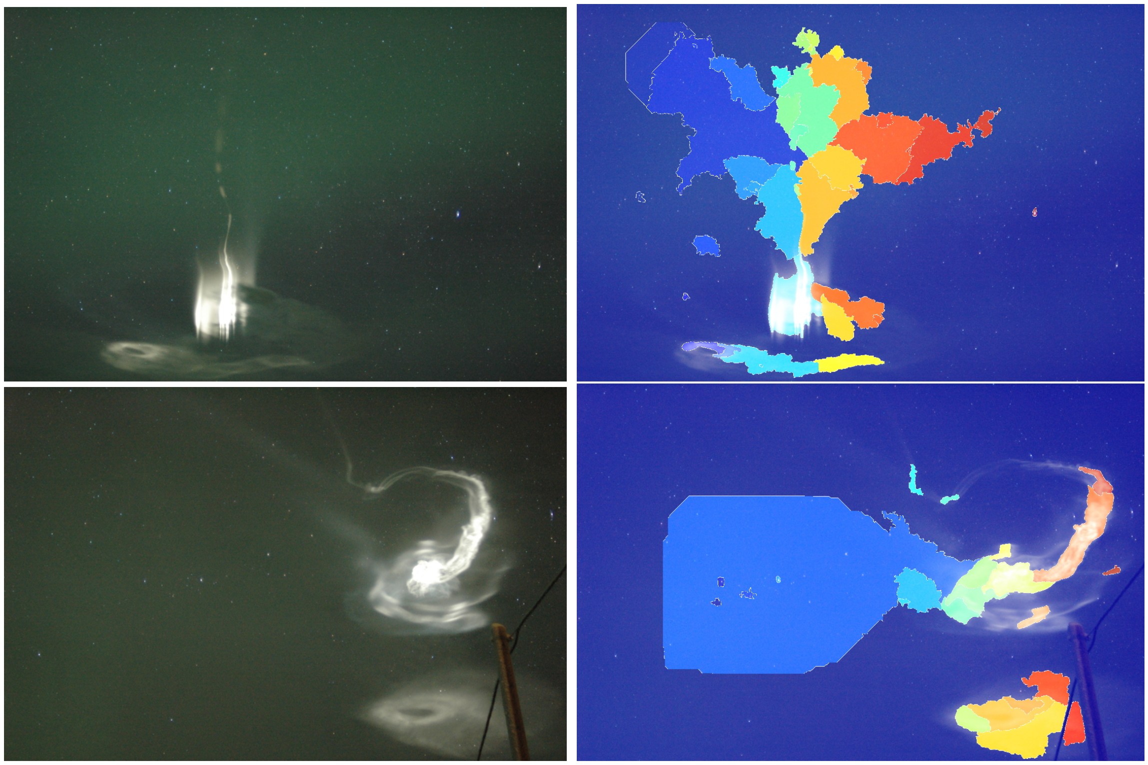

Figure 2.9: Watershed Segmentation Sample Results

missed entirely.

In this case, watershed segmentation clearly does not provide useful results. Watershed is suited to images with less variation. Gradient magnitudes of images do show the edges of TMA well, but the selection of the foreground and background markers that are required to prevent oversegmentation is not simple and results in incorrect identification of regions.

A more fundamental problem with segmentation in general is that segmentation identifies regions, which would then have to be thinned to lines, since the goal is a single-pixel-wide trace. There are many ways to thin an image to a single line, including finding the skeleton and the general thinning operation. These add unnecessary complications to the TMA detection process.

An alternate approach to the TMA detection problem is to look for lines, and not regions, from the outset. This approach, however, requires a minimal amount of user input to seed the chosen algorithm, so it can be considered more user-directed than automated.

The canonical computer vision tool for determining lines and contours is colloquially known as "snakes." More formally referred to as an active contour, a snake is an "energy-minimizing spline guided by external constraint forces and influenced by image forces that pull it toward features such as lines and edges" [9]. Snakes can be used to find edges and maxima of regions.

As with watershed segmentation, the snakes method does not prove successful for TMA detection. Snakes are more suited to edge detection than peak detection. In addition, the rough and nonuniform nature of the TMA trail leaves it without a clear maximum that can be traced along the trail.

A brute-force alternative to snakes based on peak detection proved to be the most successful option for TMA identification.

2.3.1 Peak Detection Algorithm

Like snakes, the selected peak-detection algorithm is user-directed. It is based on a set of seed points along the TMA trail. The seed points are user supplied but do not need to be extremely accurate or dense as the algorithm corrects for smaller errors in the seed points. Figure 2.10 shows a downleg image with an example set of seed points. Note that there are more seed points in areas of the trail that have finer

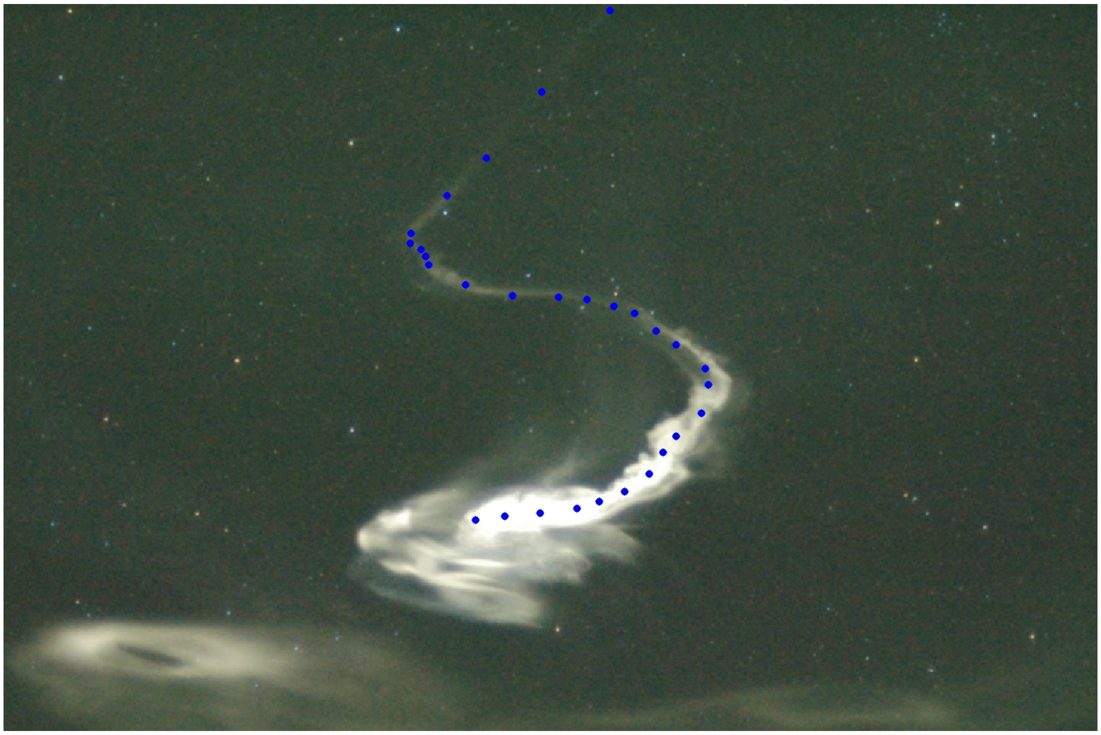

Figure 2.10: Sample set of Seed Points

structure, while straight sections have fewer. A MATLAB GUI has been written to simplify this procedure. It allows a user to load an image, click to place points, and then save the points to a data file.

Prior to any actual processing, the image in question is converted to grayscale by discarding the green channel as above. A median filter is then applied to the resulting grayscale image. Median filtering is a nonlinear operation that is applied on a pixel-by-pixel basis. Each pixel is replaced by the median gray value of the surrounding region. In this case, the region is defined to be the twenty by twenty pixel box surrounding the pixel in question. The result of conversion to grayscale and median filtering is shown in Figure 2.11. Conversion to grayscale serves to discard any aurora, and median filtering smoothes rough areas in the image, like stars and

Figure 2.11: Trail Image Converted to Grayscale and Median Filtered

turbulent features in the trail.

Given a set of seed points, the next step is to determine a piecewise-linear curve by "connecting the dots." A simple linear interpolation is used to evenly space points approximately one pixel apart between each consecutive pair of seed points. The result of this procedure is a new denser set of seed points. Figure 2.12 shows the result of applying this interpolation process to the seed points in Figure 2.10.

The new (interpolated) seed points trace out the entire area of interest in the image, including the gaps between discrete puffs that do not actually contain TMA. The next step is to find a one-dimensional slice through the image at each interpolated point, perpendicular to the trail. Again, a simple one-dimensional linear interpolation is

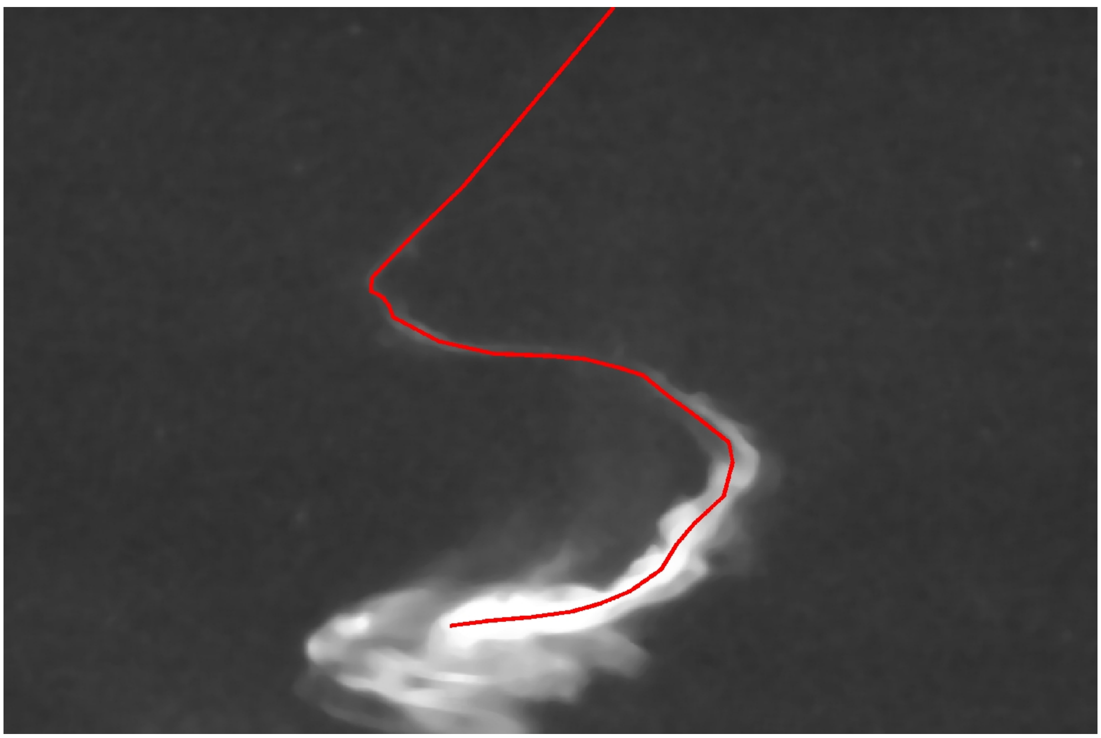

Figure 2.12: Result of Interpolating Seed Points from Figure 2.10

used to determine the coordinates in the image between the two endpoints of the slice. These endpoints are calculated on a point-by-point basis by finding the local slope along the trail and then calculating the negative reciprocal to determine the slope of a perpendicular line. Given this slope and the desired length of the slice (60 pixels in this case), it is then possible to determine the endpoints for the slice using the points-slope form of the equation of a line. Nearest-neighbor interpolation is used to determine the gray values of each point in the slice. Figure 2.13 shows a plot of a sample one-dimensional slice and its location in the image. The slices associated with all interpolated points are precalculated and stored.

Once the slices have been found, the next step is to find the peaks in each slice. These peaks are considered to the location of the TMA along the slice. It is assumed that the TMA peaks in brightness at the center of the trail. The "Peak Finding and Measurement" [17] routine written by Tim O'Haver is used to accomplish this task. The routine has several input parameters including slope threshold, amplitude threshold, smoothing width, and fit width.

Prior to calling the actual peak-finding routine, two additional parameters are used to determine if peak-finding is necessary at all. First, the number of fully white (gray value 255) pixels is determined. If there are more than a saturation threshold, peak finding is not performed and the position of the TMA in the slice is determined from the average location of the saturated pixels (i.e. the center). This is used because the peak finding code produces spurious results for curves that have flat-topped due to saturation. If the slice has fewer than the saturation threshold of white pixels, the standard deviation is then calculated. If the standard deviation exceeds a threshold value, the slice is passed to the peak-finding routine. If the threshold condition is not

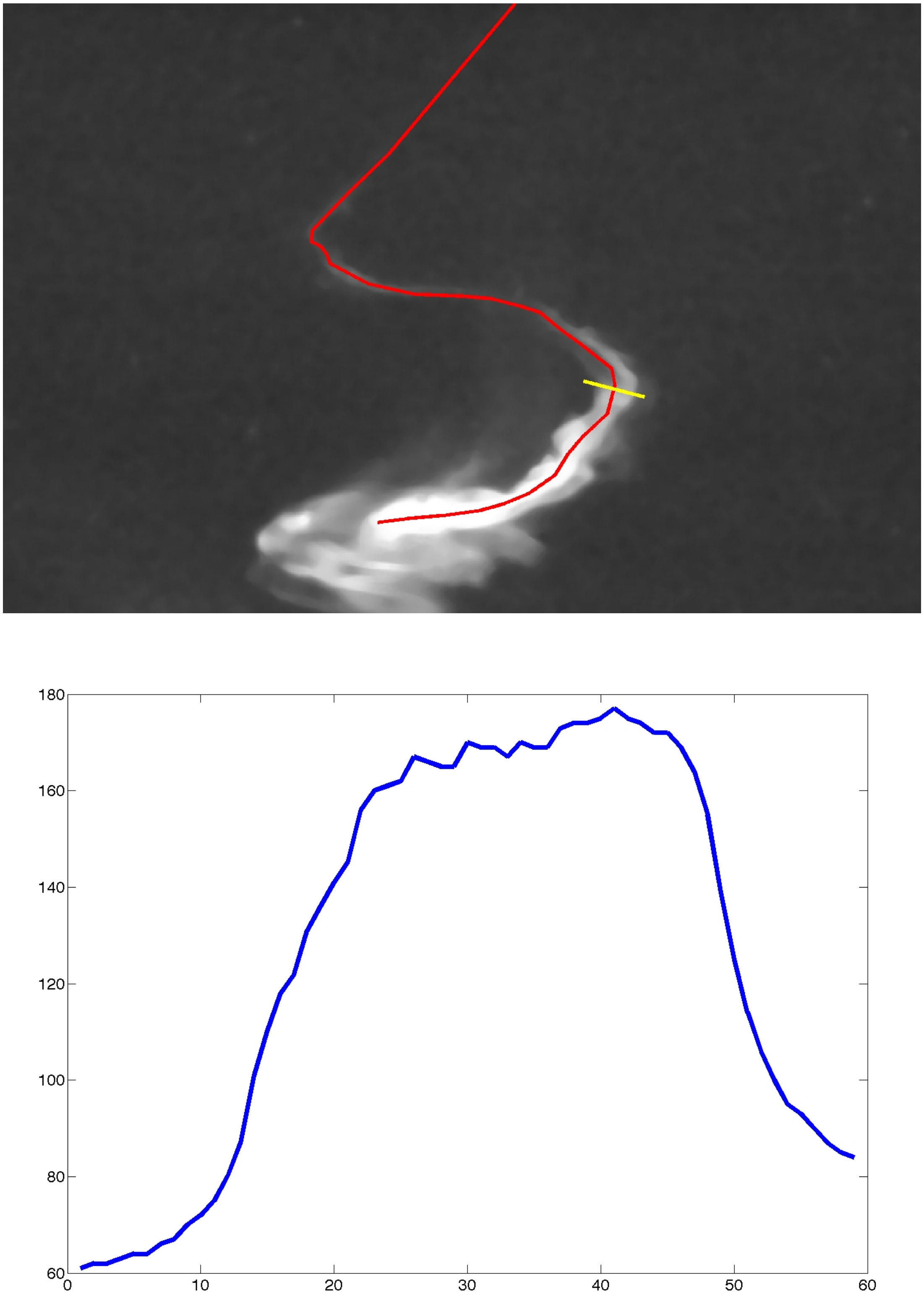

Figure 2.13: One-Dimensional Slice from Figure 2.12 and Slice Location

met, the slice has little variation and is assumed to pass through an area where there is no TMA present. This serves to eliminate the sections of empty sky between puffs of TMA.

If none of these conditions are met, the slice is passed to the peak-finding routine, *findpeaks*, which works by smoothing the input curve and then looking for peaks by searching for "downward zero crossings in the first derivative." [17] The candidate peaks are then checked against the input parameters. The smoothing and fit width parameters are set to the same value. Smoothing width is used by the internal smoothing routine to eliminate noise. The fit width is the number of pixels to use in the unsmoothed peaks to determine peak amplitude and height. The slope and amplitude thresholds are used to cull spurious peaks that are not steep or tall enough to be considered. All of the above operations take place within the peak-finding routine. [17]

Figure 2.14 shows the result of the peak-finding-based TMA detection algorithm on two different images. The red dots are detected TMA and the blue line represents the interpolated seed points. The top image represents the worst case results. The trail is fairly irregular due to turbulence, which is reflected in the roughness in the detected points. The lower image shows a case where the algorithm results in more consistent results. The gaps in the trail caused by puffing are skipped correctly and the overall curve is smoother. More than half of the trail shown is above the turbopause, which results in smoother and less featured TMA trail. In both cases the results are sufficient to feed the regularization algorithm. Note that in both images the detected TMA points deviate from the seed line as appropriate to actually follow the trail. As with the other image processing tasks, a MATLAB GUI has been written for the TMA detection algorithm. The GUI provides an efficient way to tweak the peak finding parameters on an image-by-image basis.

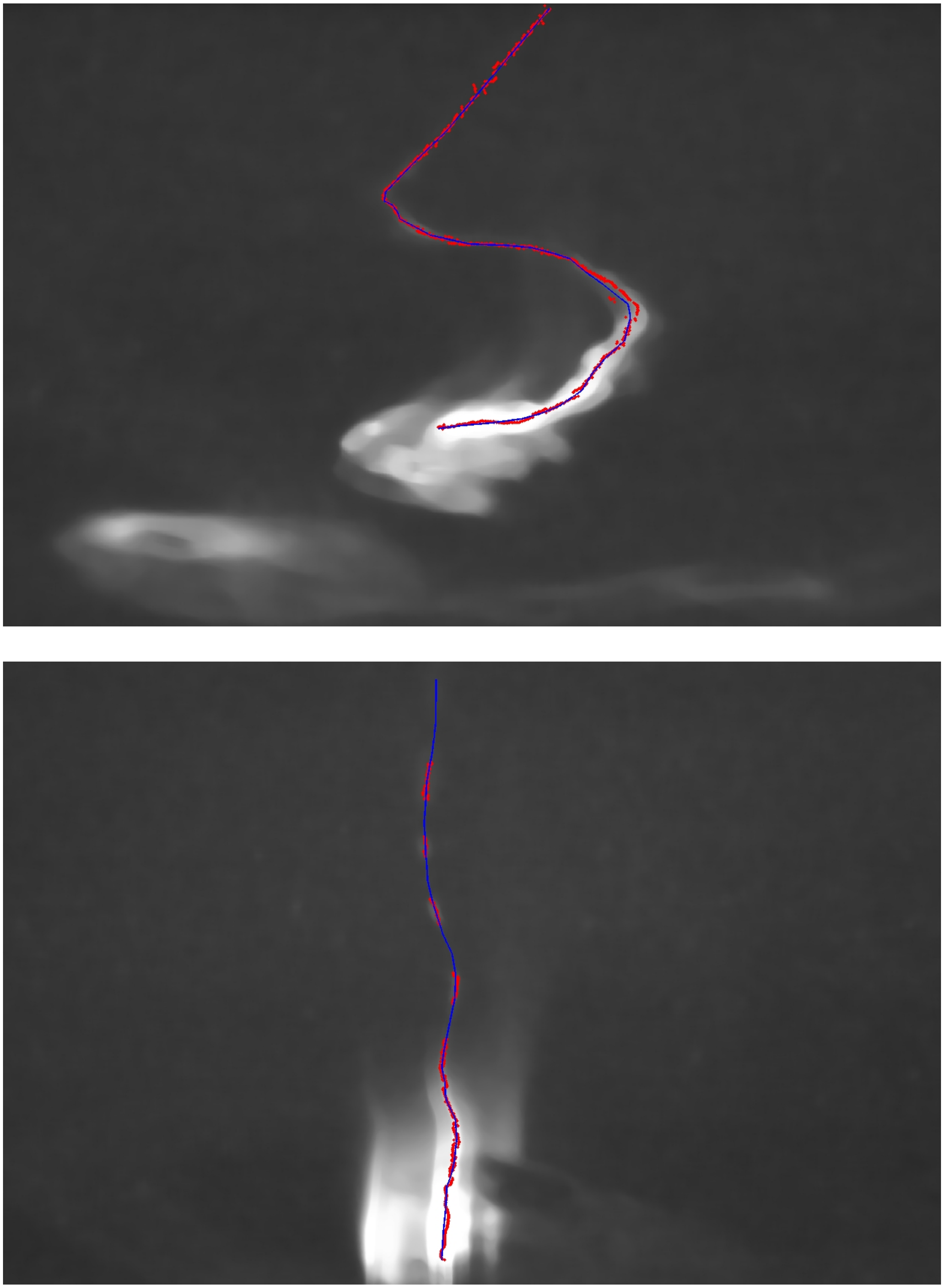

Figure 2.14: Results of TMA Detection

Chapter 3

Triangulation

3.1 Overview

Triangulation refers to the process of determining the location of a target based on measurements from two known locations. If the angles to the target from the known positions and the baseline between the known positions are both known, it is then possible to determine the absolute location of the target.

In this case, triangulation refers to the determination of the position of TMA clouds from photographs taken at two or more locations. Techniques related to and derived from the above description are developed.

3.2 Methodology

There are a number of ways to approach the problem of triangulation. Computer vision provides a tool called epipolar geometry that allows for the computation of location based on an explicit geometrical relationship. Another method is based on projecting lines of sight from one camera into other images. The latter method was found to be better suited to this specific triangulation task.

3.2.1 Epipolar Geometry

Hartley and Zisserman [5] describe epipolar geometry as "the intrinsic projective geometry between two views. It is independent of scene structure, and only depends on the cameras' internal parameters and relative pose." It is typically used in computer vision with stereo camera pairs to determine the three-dimensional location of objects. The fundamental matrix F and essential matrix E contain all the parameters needed to calculate the position of an object in both cameras' field of view. The eight-point algorithm can be used to calculate the fundamental matrix from a set of 8 corresponding points in the image pair.

The conditions under which the eight-point algorithm is typically used differ greatly from the camera setup used for triangulation. Normally, the cameras are fairly close together and placed so that their focal planes lie in the same plane. The large distance (on the order of 100 km) between cameras and arbitrary camera pointing angles complicate the problem. In this case, the fundamental and essential matrices must be directly calculated from camera parameters, rather than estimated from common points in the scene as is usually the case. One final issue is that eight-point algorithm is typically utilized on small scales like indoor environments. The area in question in this case covers hundreds of square kilometers of sky in northern Alaska.

Given the above difficulties and the atypical nature of the camera positions, a triangulation procedure based on epipolar geometry calibrated by the eight-point algorithm is not suitable for this situation. Other, more direct methods are more feasible.

3.2.2 Direct Computation

Rather than a mathematical calculation involving the eight-point algorithm used to calibrate epipolar geometry, the triangulation method chosen directly calculates and projects lines of sight into images. This method uses coordinate systems and transformations taken from astronomy to project lines of sight from one camera into the other cameras' images.

3.3 Challenges

There are several properties of the photographs and the experiment that pose additional challenges. In general, it is not always possible to match discrete features in each image. There may not be enough identifiable features due to camera location or smoothness of trail features. This therefore rules out a simple automatic matching of trail features using templates or other computer vision techniques.

Two approaches that counter these challenges have been implemented. One is manual and relies on user input, while the other automatically matches points generated by the TMA detection algorithm using a minimization approach.

3.4 Manual Triangulation

The manual triangulation procedure requires a significant amount of relatively tedious user input. A MATLAB GUI has been written to assist in this procedure. The basic algorithm consists of choosing a point of interest on the TMA trail in the first image, projecting the line of sight from the first image into the second image, and then choosing the point at which the projected line of sight crosses the TMA trail in the second image. This procedure is repeated until the required number of corresponding points have been collected. The line of sight projection procedure is detailed below in section 3.4.1. Figure 3.1 illustrates this process for a few pairs of corresponding points. The final set of corresponding points is then processed to determine the latitude, longitude, and altitude of the points along the TMA trail.

3.4.1 Line of Sight Projection

The line of sight to a feature in one image passes through the camera's center of projection and extends to infinity. When projected into the image, the entire line appears as a single point. If the line of sight is instead projected into another camera pointed at the same feature, it does not appear as a single point, but rather, as a line. This occurs because the line does not pass through the second camera's center of projection. Figure 3.2 illustrates the line of sight projection procedure.

Following the flow in Figure 3.2, projecting a line of sight begins with the image coordinates (pixels or mm) of a point of interest in a photograph from site 1. The image coordinates are converted to standard coordinates using the image's plate constants. From standard coordinates, it is then possible to convert to equatorial coordinates if the right ascension and declination of the image center are known.

Equatorial coordinates can then be directly converted to geocentric coordinates (Cartesian centered on the center of the earth). Equation (3.1) illustrates this con-

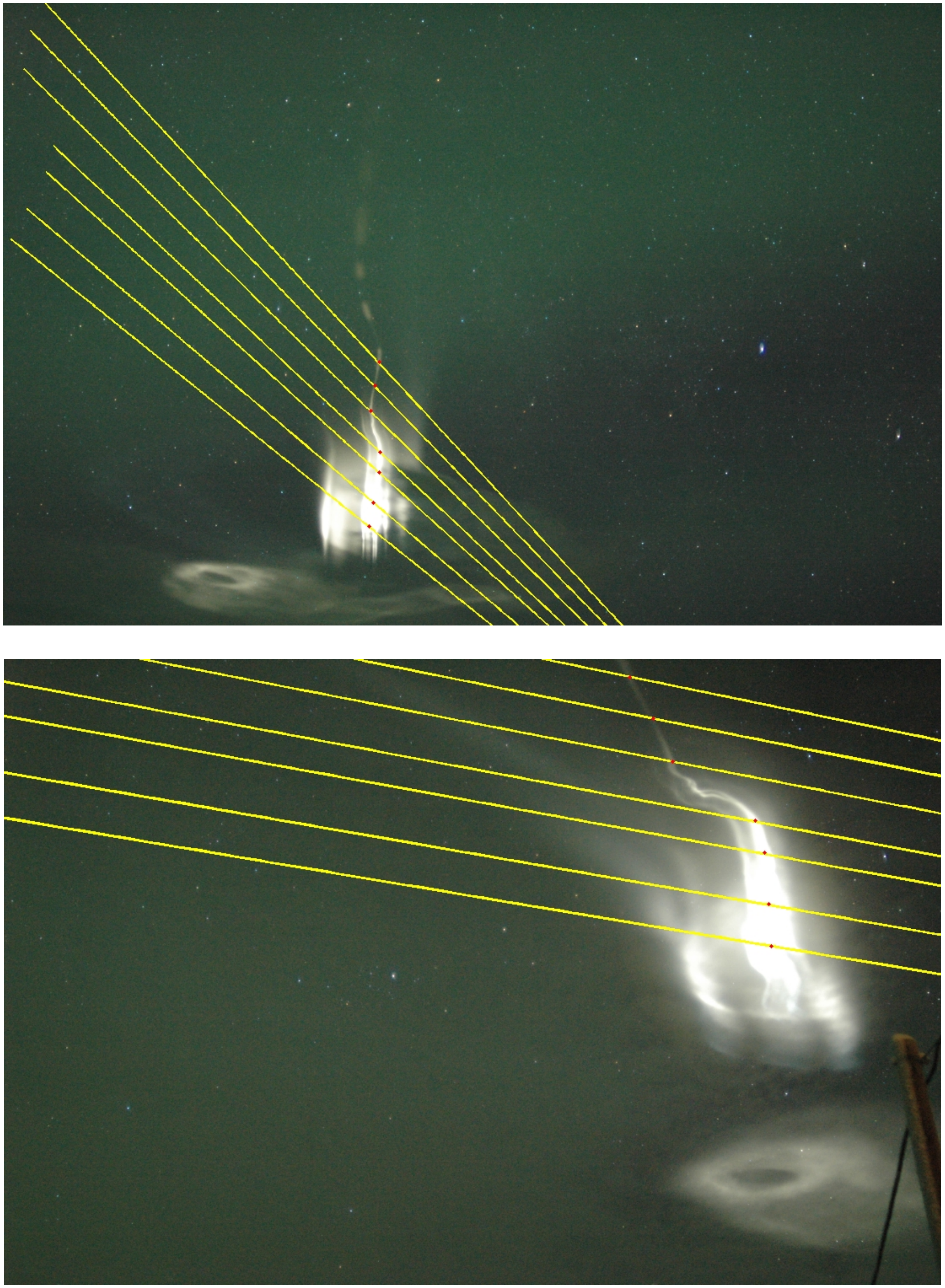

Figure 3.1: Manual Triangulation Point Pairs and Corresponding Lines of Sight

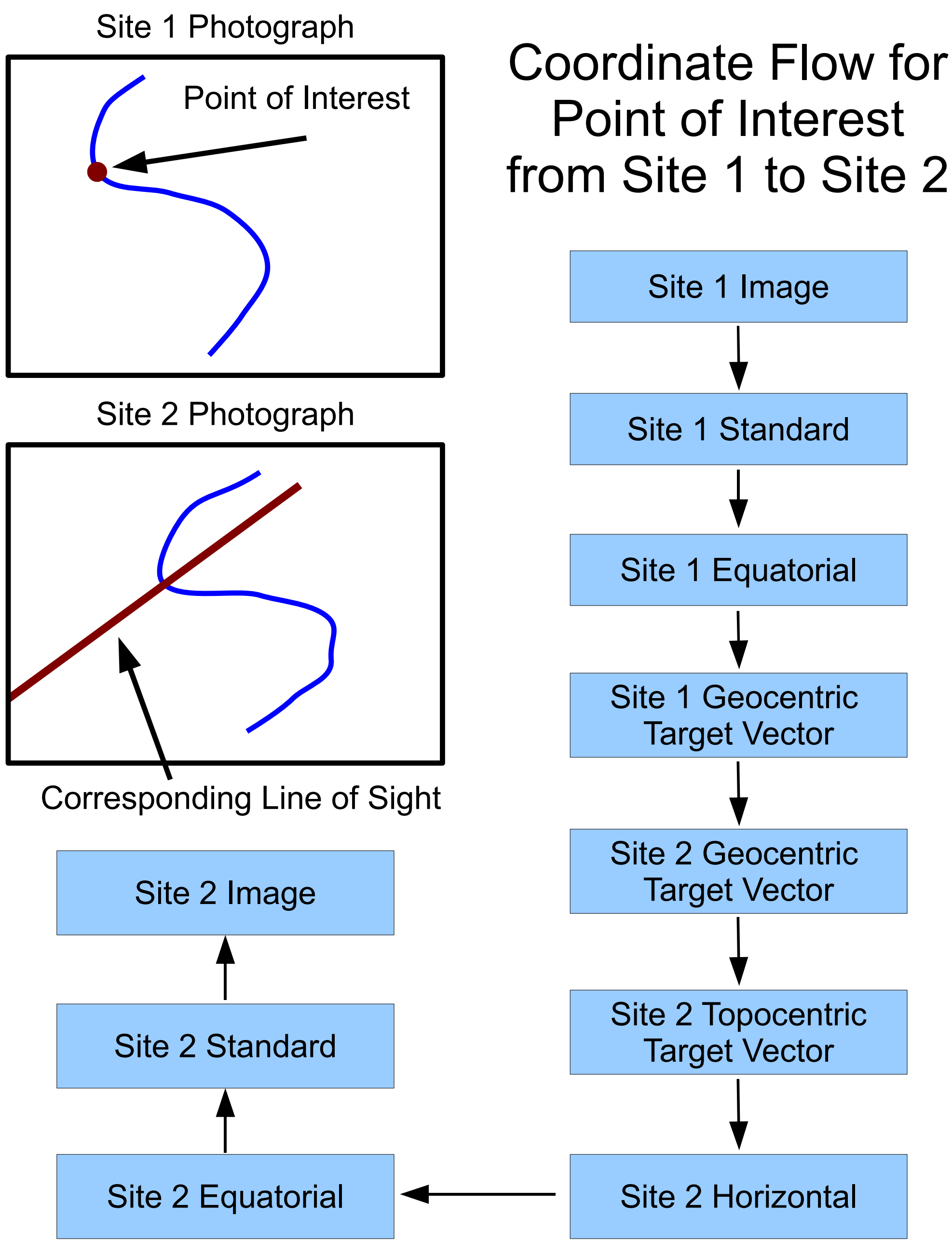

Figure 3.2: Coordinate Conversion Flow for Line of Sight Projection

version,

$$
\begin{aligned}
X &= \cos(\delta)\cos(\alpha - \Phi) \\
Y &= \cos(\delta)\sin(\alpha - \Phi) \\
Z &= \sin(\delta)
\end{aligned} \tag{3.1}
$$

where (α, δ) are the equatorial coordinates to be converted, (X, Y, Z) are the resultant geocentric coordinates and Φ is the local sidereal time. The result is a single vector pointing from the camera to the point of interest. Along with the geocentric coordinates of site 1, this vector is then used to generate a geocentric target vector. The target vector consists of a series of points spaced one kilometer apart along the line from site 1 to a point 400 kilometers out from the camera.

This target vector is then converted to site 2's geocentric coordinates by subtracting the location of site 1 and adding the location of site 2. Knowledge of site 2's latitude and longitude are then used to convert the points in the target vector to site 2's topocentric coordinate system (cartesian, centered on the camera).

The topocentric coordinates are then converted to horizontal coordinates (azimuth and elevation) using (3.2),

$$
\begin{aligned}
az &= \arctan\frac{Y}{X} \\
h &= \arccos\frac{X}{\sqrt{Y^2 + Z^2}}
\end{aligned} \tag{3.2}
$$

where (az, h) are azimuth and elevation and (X, Y, Z) are topocentric coordinates. The horizontal coordinates are next converted to equatorial, then standard, and finally image coordinates (using the second photograph's plate constants). At this point, what began as a single point in the image from site 1 is now a line in the image from site 2.

3.5 Automatic Triangulation

While the manual triangulation algorithm relies on user input, it is possible to automate the process. Rather than collecting mouse clicks to indicate points of interest on the TMA trail, the automatically detected TMA points are used instead. As in the manual triangulation procedure, the goal is to match up pairs of points from the two images.

Automatic triangulation, in essence, solves a minimization problem: which pair of TMA points results in the minimum distance between their line-of-sight vectors at closest approach? Ideally, line-of-sight vectors from corresponding points would intersect, but this is generally not the case due to the level of precision required. Figure 3.3 illustrates the automatic triangulation procedure.

For each of the two images, the image, plate constants, image center coordinates, and TMA points are loaded. The image filenames are then used to look up sensor size (in mm), Julian Date, Greenwich mean and local sidereal time, and camera site latitude and longitude. The geocentric coordinates of the cameras, conversion matrices for geocentric to topocentric coordinates, and look direction vectors are then calculated. Finally, the geocentric target vectors are precalculated for each TMA

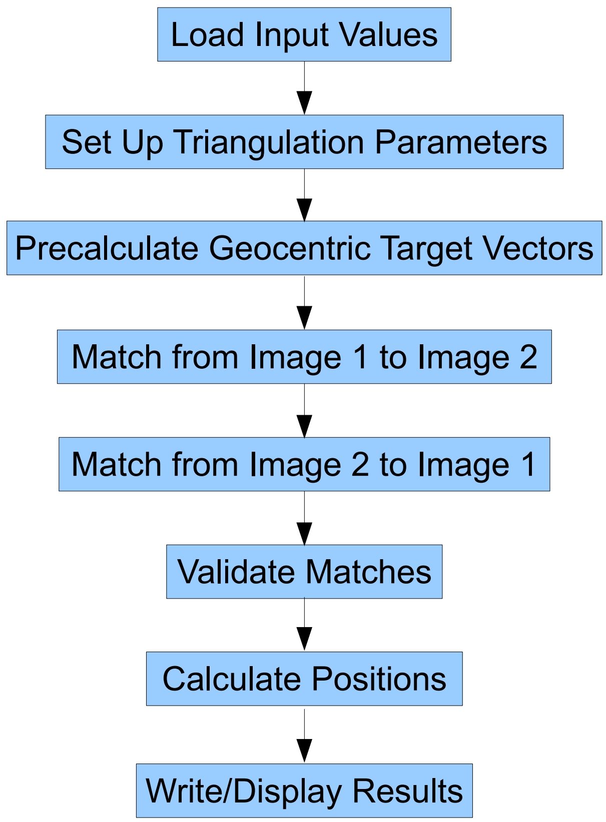

Figure 3.3: Automatic Triangulation Procedure

point in both images. These vectors point from the camera site along the line of sight to each TMA point.

First, points are matched from the first image into the second. For each TMA point in image 1, the closest approach distance is calculated for each point in image 2 using the procedure derived in Appendix D. The point in the second image that produces the best minimum distance is saved as a match (subject to a maximum distance threshold) The matching procedure is then repeated, but this time by matching points from image 2 to image 1. This produces an additional list of matches.

After matching in both directions, a validation procedure is used to prevent spurious results. A pair of points is retained only if it was discovered in both searches. In other words, matching from image 1 to image 2 must have found the exact same pair as matching from image 2 to image 1.

Position calculation in automatic triangulation is the same as in manual triangulation and is described in section 3.6.

Several plots are used to display the results of automatic triangulation to assist in determining the validity of the result. First, the two input images are displayed with the matched TMA points plotted on them. The TMA points are plotted in a repeating sequence of colors to assist in identifying pairs between photos. Figure 3.4 shows two such images for an upleg image pair. In addition, a combined plot is made with the two images stacked and vectors drawn between the matched point pairs. An example of this type of plot is shown in Figure 3.5.

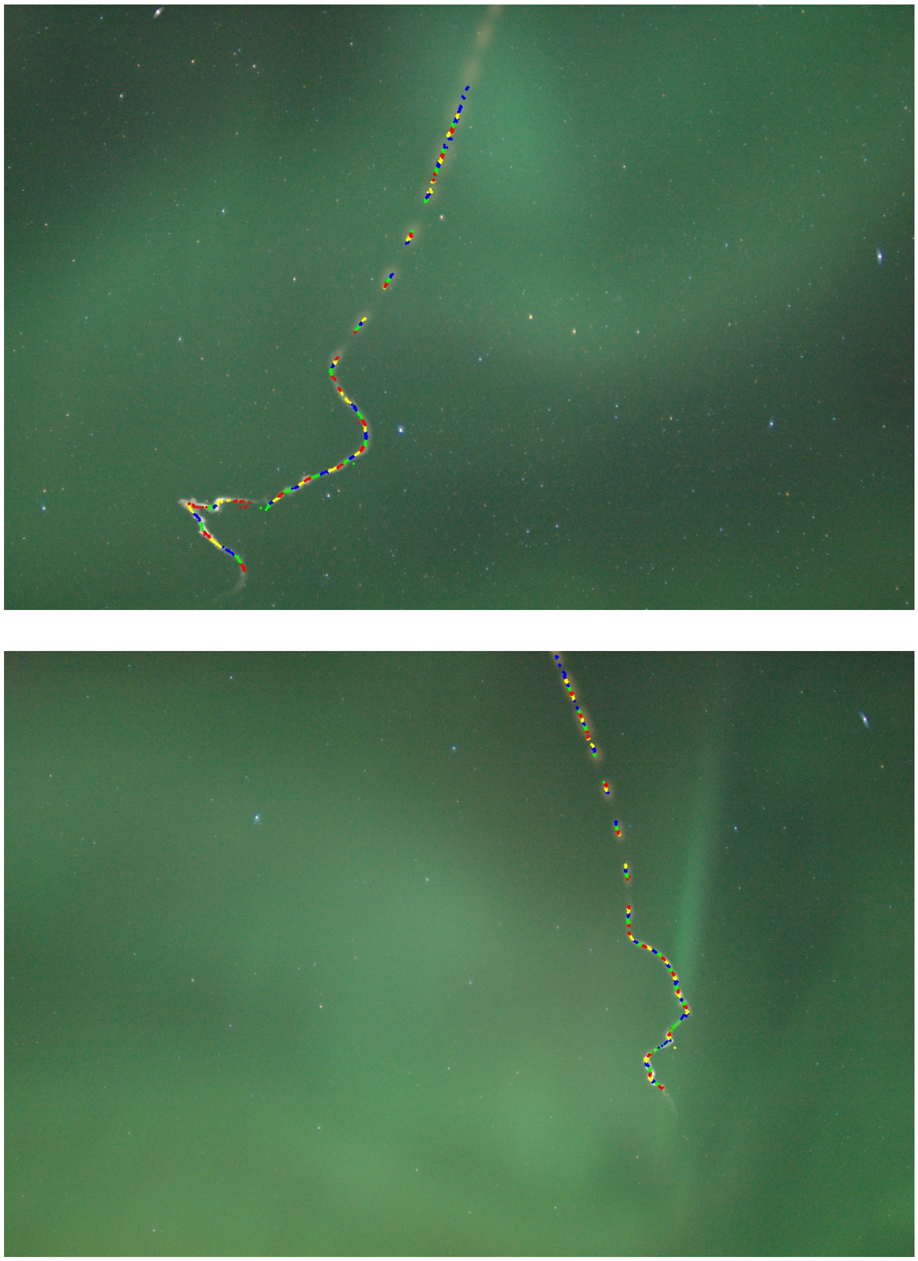

Figure 3.4: Automatic triangulation results for an image pair from HEX II

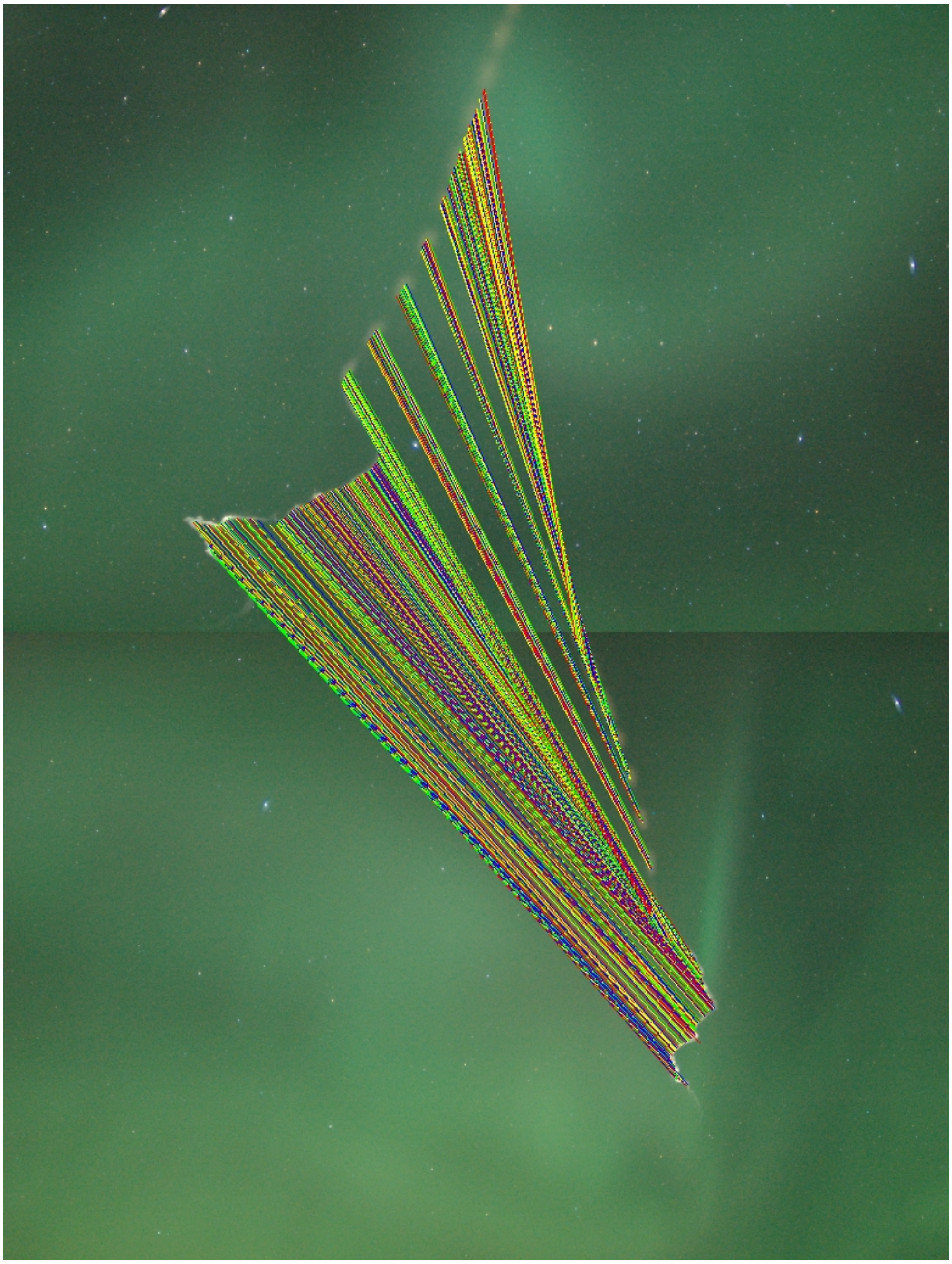

Figure 3.5: Automatic triangulation results with lines connecting corresponding points

3.6 Position Calculation

Given a pair of points in simultaneous images that mark the same feature, it is possible to determine the location in three-dimensional space of the feature. The procedure derived in appendix D is used to determine the point of closest approach in geocentric coordinates. This point is then converted to latitude (geocentric) and longitude as well as a height above sea level.

Chapter 4

Wind Determination

4.1 Overview

Traditionally, a tracking method based on triangulation of pairs of simultaneous images has been used to calculate winds. A regularization procedure is implemented that eliminates the need for pairs of simultaneous measurements. Other more mathematical estimation tools were considered but discarded due to the nature of the wind-determination problem.

4.1.1 Assumptions

There are several major assumptions made when determining neutral winds from photographs of TMA releases. The most restrictive of these requires that the vertical wind be either zero or negligible (a few tens of meters per second at most). This assumption means that a TMA cloud at a given altitude in one image will be at the same altitude in any other image. In addition, the wind determination procedures all assume a constant linear change in the position of TMA with respect to time. This requires the complementary assumption that the winds are constant over the lifetime of the TMA trail (5 to 30 minutes). Finally, each altitude is assumed to be independent from all other altitudes and can therefore be evaluated without regard to the parameters at other altitudes.

Due to the short lifetime of the TMA trail and the relatively small observed vertical winds at the altitudes in question (80 to 150 km), these assumptions prove to be reasonable and do not adversely affect the quality of the resulting wind profiles.

4.1.2 Other Methods

Several more mathematical estimation tools were considered before the final regularization method was chosen. The Kalman filter, a Bayesian estimation tool first described by Kalman in 1960 [8], is an obvious choice but is not suitable to this application since it requires a linear transformation from the state of the system (position and velocity of a TMA puff) to the measurement (photograph). This condition is not met due to the nature of the coordinate systems and conversions involved. The extended Kalman filter, which uses a local linearization of the transformation, would be a possible solution to this problem, but the transformations are not easily linearized without incurring large errors. The particle filter (also known as sequential Monte-Carlo methods) eliminates the linearity requirement but is also unsuitable. Both of the above methods assume that the quantity being estimated changes with time, which is not the case in this problem. In addition, there are, in general, not enough data points to support the estimation of a time-varying quantity.

4.2 Tracking Method

The traditional, tracking-based method, uses multiple pairs of simultaneous images from different camera sites. Each pair of images, after triangulation, gives the position of the trail as a function of altitude. Multiple pairs of images then give the position of the trail as a function of both altitude and time. From this data, a linear least squares fitting procedure is used to determine wind velocity at each altitude. Errors are calculated from the deviation from the linear fit at each altitude.

4.3 Regularization Method

The regularization method is essentially a search over a four-dimensional parameter space for each altitude. The parameters are the initial position (latitude and longitude) and wind vector (zonal and meridional wind). Zonal refers to the east-west direction and meridional refers to the north-south direction (along a meridian). The algorithm then determines the best initial position and wind vector at each altitude using a genetic algorithm.

4.3.1 Input Parameters

The algorithm uses several required parameters and one optional input parameter. Required parameters include the images being processed, their plate constants, and the pixel coordinates of their detected TMA. Also needed are the time and date, latitude and longitude of the camera sites, and the seed positions (initial latitude and longitude at each altitude). Seed wind values are optional but help the algorithm to converge more quickly. Seed positions can be determined by the automatic triangulation procedure described above, and seed winds can come from a variety of sources,

Parameter	Δ Zonal	Δ Meridional	Δ Latitude	Δ Longitude
Value	-22.74	12.71	0.00024	0.0041

Table 4.1: Sample Chromosome for Genetic Algorithm

including traditional triangulation, models, and radar tracking data for the rocket.

4.3.2 Genetic Algorithm

The heart of the regularization procedure uses a genetic algorithm to search the parameter space. A genetic algorithm is in essence a directed random search that borrows concepts and nomenclature from biological genetics. The search consists of a sequence of generations, each made up of multiple chromosomes. In the case of the regularization algorithm, the chromosome has four values, each representing a perturbation from the seed latitude, longitude, zonal wind, or meridional wind. Table 4.1 illustrates a sample chromosome.

The actual search procedure for a genetic algorithm follows the principle of the survival of the fittest. The chromosomes of each generation are evaluated to determine the ones with the most desirable characteristics. The best chromosomes are saved and the remainder are discarded. Typically, the retained chromosomes are used to help generate the next generation. They can be bred if the chromosome format and problem allow an easy method of blending. Otherwise, the saved chromosomes can be mutated by adding random noise, or completely unrelated chromosomes can be introduced to deepen the gene pool. As described below, the regularization algorithm uses all of the above methods. Once the next generation has been created, it too is evaluated, and the cycle is repeated. This continues until a stopping condition is reached, typically by meeting a convergence threshold or a maximum generation count.

4.3.3 Implementation

The regularization procedure is implemented as a set of MATLAB scripts. Specifically, two versions have been developed, one serial and one parallel. The serial implementation sequentially determines the best parameters at each altitude and is designed to run on a single processor. The parallel version computes parameters at each altitude simultaneously and is intended to be run on a cluster.

The serial version runs within the MATLAB GUI and provides a graphical representation of the output in addition to numerical results. This method runs relatively slowly due to the overhead of the MATLAB user interface. Also, sequential calculation of each altitude's parameters is inefficient in general due to the assumption of independence between altitudes. There is no reason other than MATLAB's lack of parallel processing tools to calculate the parameters at each altitude in any specific order.

The parallel implementation eliminates this inefficiency by calculating parameters at all altitudes simultaneously. Since MATLAB itself lacks parallelism beyond the simple multithreading of basic calculations, multiple instances of MATLAB must be used to accomplish any parallel speedup. Thus, a shell script is used to fill in the parameters for each altitude in a template MATLAB script and submit a job to a cluster for each altitude. This results in a significant speedup, especially since the batch-processing mode of MATLAB used on the cluster is significantly faster than the desktop version. A 500,000-generation-per-level regularization can be run on a cluster in approximately twelve hours, while the serial version, running in the

MATLAB desktop would take on the order of weeks to months.

4.3.4 Procedure

Figure 4.1 outlines the steps of the regularization algorithm, which are described in detail below.

4.3.4.1 Load Input Values

This step loads the seed wind and position profiles. Seed winds are optional, but allow the genetic algorithm to converge faster since they provide an estimate of the actual values. Without seed winds, the algorithm has to start from scratch with the winds set to zero and may take longer to converge to the actual values. In addition, the serial or parallel implementation is selected, and, in the case of the parallel implementation, the altitude to be processed is set.

4.3.4.2 Interpolate and Find Overlap of Seed Values

The seed wind and position profiles are not necessarily sampled at the same intervals nor do they normally cover the same altitude ranges. This step uses the MATLAB command *interp1* to resample and interpolate the profiles to half-kilometer steps in altitude. *interp1* in this case is set to use the *pchip* (piecewise cubic Hermite interpolating polynomial) mode as it gives the best results.

After interpolation, the next step is to determine the altitude ranges where the seed wind and position profiles overlap since both values are required by the algorithm. Of course, if there is no seed wind, then the overlap region is the entire altitude range of the position profile.

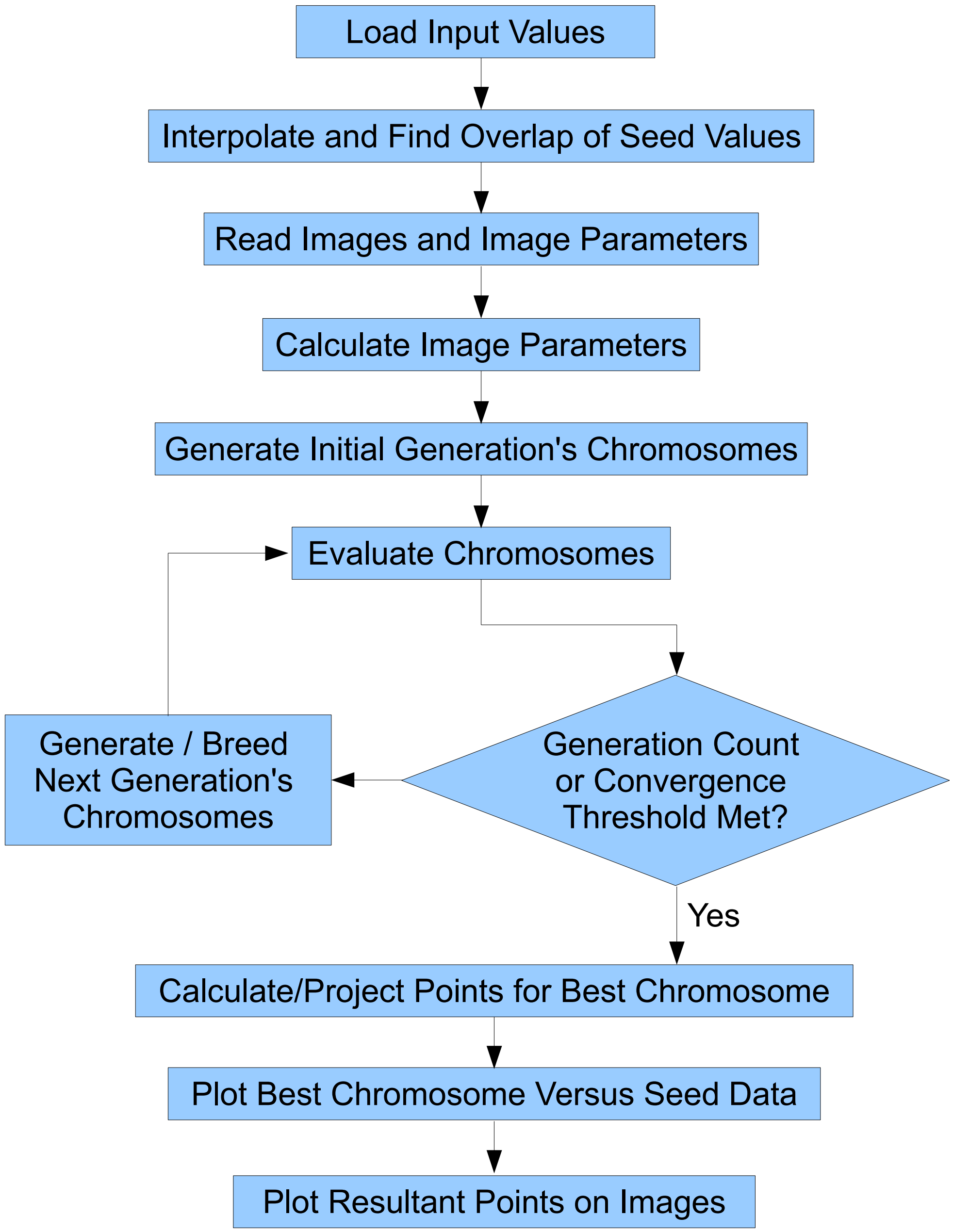

Figure 4.1: Regularization Procedure Flowchart

4.3.4.3 Read Images and Image Parameters

Next, the images containing TMA are loaded as well as their parameters. These parameters include plate constants, image centers (both equatorial and azimuth/elevation), and the list of TMA point coordinates.

4.3.4.4 Calculate Image Parameters

Image filenames are used to determine a set of parameters using a lookup table. These values include sensor size (in mm), Julian Date, Greenwich mean and local sidereal time, and camera site latitude and longitude. All of this information is then used to determine the geocentric coordinates of the camera site as well as the conversion matrix between geocentric and topocentric coordinates.

4.3.4.5 Generate Initial Generation's Chromosome

As implemented in the regularization procedure, each generation of the genetic algorithm has twelve chromosomes. One of the first generation's chromosomes is set to the seed position and wind values. The remainder are randomly selected from a range around the seed values.

4.3.4.6 Evaluate Chromosomes

At this point, the chromosomes of the current generation must be evaluated to determine which provide the best set of parameters. The chosen metric is an error distance, measured in pixels, on the TMA images themselves. For each chromosome, the initial position and wind velocities are used to calculate the location of TMA for each time an image is available. This position (in geocentric coordinates), is then projected into its corresponding image. The minimum distances from these projected points to the TMA points identified in the image are then calculated. The chromosome with the lowest sum of minimum distances over all TMA images is considered the best solution.

4.3.4.7 Generation Count or Convergence Threshold Met

There are two possible termination conditions for the search: generation count or convergence threshold. Generation count means that the genetic algorithm stops searching after a fixed number of iterations. Using a convergence threshold, however, means that the search will continue until a predetermined minimum distance sum is met. Usually the threshold stopping condition is combined with a maximum generation count to prevent an infinite loop in the situation where no solution less than the threshold is possible.

In the case of the parallel version of the algorithm, the program terminates upon reaching a stopping condition. The serial version, however, continues to the next altitude when the genetic algorithm at the current altitude terminates.

4.3.4.8 Generate / Breed Next Generation's Chromosomes

If the algorithm has not reached a stopping condition, the next generation of chromosomes is now calculated. The two best chromosomes from the previous generation are used as the parents of the next generation. The two parents are used to breed six children. In this case, breeding consists of taking the randomly weighted average of the parents. Two additional chromosomes for the next generation are generated by mutating the two chosen parents by adding random noise. Finally, two unrelated random chromosomes are generated to increase the variability of the gene pool. Table 4.2 illustrates this procedure.

Chromosome	Generation Method
1	Best chromosome from previous generation (parent 1)
2	Second best chromosome from previous generation (parent 2)
3	Child: (rand) $\times$ (parent 1) + (1 $-$ rand) $\times$ (parent 2)
4	Child: (rand) $\times$ (parent 1) + (1 $-$ rand) $\times$ (parent 2)
5	Child: (rand) $\times$ (parent 1) + (1 $-$ rand) $\times$ (parent 2)
6	Child: (rand) $\times$ (parent 1) + (1 $-$ rand) $\times$ (parent 2)
7	Child: (rand) $\times$ (parent 1) + (1 $-$ rand) $\times$ (parent 2)
8	Child: (rand) $\times$ (parent 1) + (1 $-$ rand) $\times$ (parent 2)
9	Random mutation of parent 1
10	Random mutation of parent 2
11	Randomly generated new chromosome
12	Randomly generated new chromosome

Table 4.2: Members of next generation for genetic algorithm

4.3.4.9 Calculate / Projects Points for Best Chromosomes

Once the best chromosome for each altitude have been determined, the program then calculates the position of the TMA (at all available altitudes) for every time that there is an image available. This procedure also calculates the error metric described above for each altitude. Note that this step only occurs in the serial version of the regularization algorithm.

4.3.4.10 Plot Best Chromosome Versus Seed Data

In addition to projecting points into the TMA images, additional plots are generated. Zonal and meridional winds are plotted versus the seed winds. The error metric (averaged over all images) is also plotted. Note that this step only occurs in the serial version of the regularization algorithm.

4.3.4.11 Plot Resultant Points on Images

The TMA locations calculated in previous steps are then projected into their respective images to produce a set of plots that show the accuracy of the chosen chromosomes. Note that this step only occurs in the serial version of the regularization algorithm.

4.3.5 Variants

Several variants of the regularization algorithm have been written. One disallows changes in the seed position, while another is more robust to TMA points drifting out of the field of view of the camera. The version that disallows changes in the seed position produces better results.

4.3.6 Smoothing

The wind profiles determined by the regularization procedure require smoothing to eliminate roughness caused by small scale variability in the detected TMA points. This variability is not present in the trail itself, but rather is a result of the TMA detection algorithm and regularization procedure. Any noise present in the input data may be present in the output. This is similar to the inverse problem of fitting a model to noisy data. A one-dimensional median filter is used with a range of plus and minus 1.5 kilometers. Similar to the two-dimensional median filter used on the TMA images, the wind speed at each altitude is set to the median value of the wind speeds in the range 1.5 kilometers above and below the altitude in question.

Chapter 5

Results

The Joule II and HEX II sounding rocket experiments were conducted from the Poker Flat Rocket Range (PFRR) in January and February 2007. The range is owned and operated by the Geophysical Institute of the University of Alaska, Fairbanks. It is located at approximately 65° 7’ N and 147° 28’ W. Situated in the Alaska time zone, AKST is 9 hours earlier than Coordinated Universal Time (UTC). The range offers several launch corridors for rocket launches, illustrated in Figure 5.1. [4]

5.1 Joule II

Launched on January 19, 2007, the Joule II experiment was designed to study Joule heating of the atmosphere at small, medium, and large scales. It consisted of two instrumented rockets and two chemical release rockets. The rockets were launched in pairs, with an instrumented rocket launched first, followed one minute later by a chemical release rocket. The two rockets were launched on approximately the same trajectories to allow for measurement of the same atmospheric volume. The second pair of rockets was launched in the same order 16 minutes later on the same

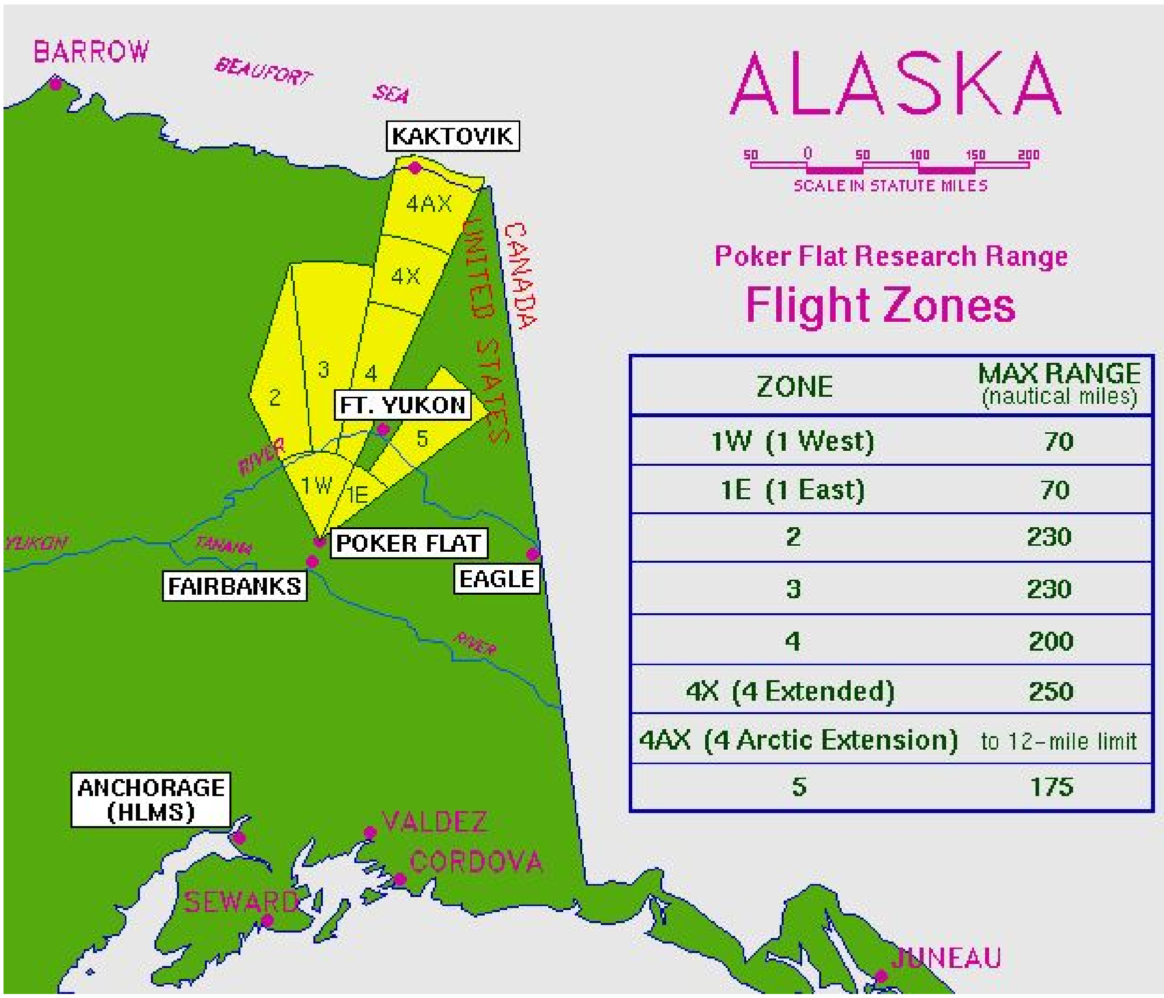

Figure 5.1: Poker Flat Research Range Launch Corridors

Camera Site	Latitude	Longitude
Poker Flat	65.119° N	147.433° W
Fort Yukon	66.559° N	145.208° W
Coldfoot	67.251° N	150.172° W

Table 5.1: Coordinates of Joule II and HEX II Camera Sites

trajectories. The repeated trajectories for the second salvo allowed for the study of temporal variations of the Joule heating. The chemical release payloads were launched on Terrier-Improved Orion sounding rockets, while the instrumented payloads flew on a Black Brant V and Black Brant IX rockets.

The chemical release rockets for the Joule II experiment were launched at 12:31 UT and 12:47 UT. The releases themselves began approximately 1 minute after launch. Three observation sites were used, the Davis Science Center located at Poker Flat, the Fort Yukon Long Range Radar Site located in Fort Yukon, Alaska, and the Coldfoot Camp located at Mile 175 Dalton Highway. Table 5.1 lists the latitude and longitude of these camera sites and Figure 5.2 shows their locations relative to the launch site.

5.1.1 Downleg 2

The downleg release from the second chemical rocket was selected for analysis because a traditional triangulation profile was available for comparison and the digital photos of the release were suited to algorithm development. Of the approximately 50 images available per camera site, 21 from Poker Flat and 21 from Fort Yukon were used in the analysis.

Figure 5.3 shows the Joule II second downleg neutral winds as calculated by the traditional triangulation algorithm. The horizontal ticks at each altitude are error

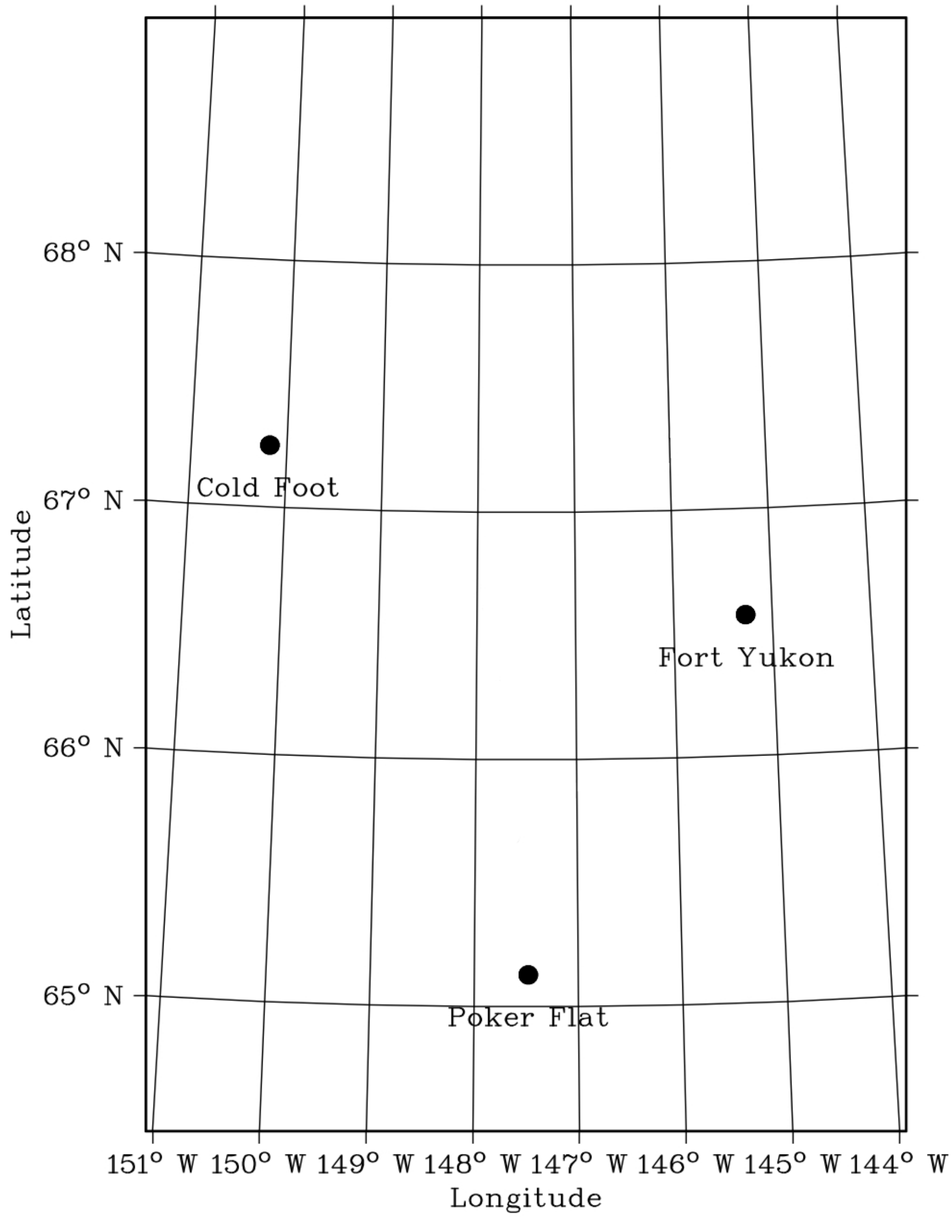

Figure 5.2: Map of Joule II and HEX II Camera Sites

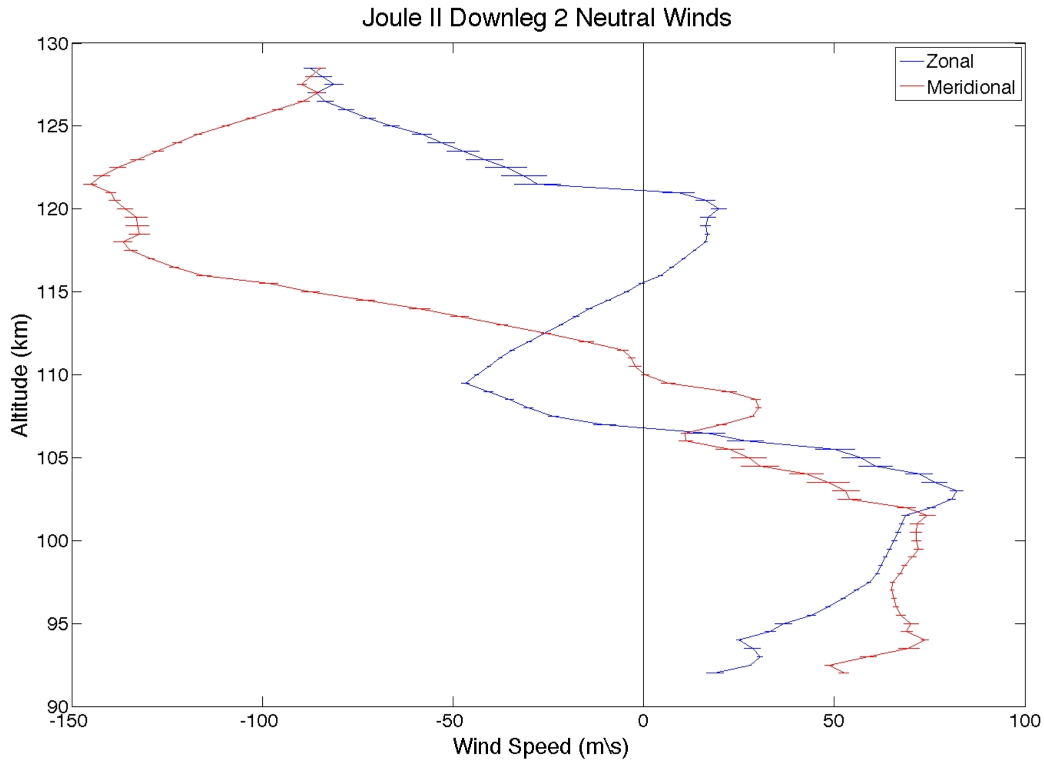

Figure 5.3: Joule II Downleg 2 Neutral Winds from Traditional Triangulation

bars, representing uncertainty in wind speed. These wind profiles were used to seed the regularization procedure.

In addition, Figures 5.4 and 5.5 show the position profiles determined using the automatic triangulation procedure, which were also used to seed the regularization. Figure 5.4 is a plot of the individual points in geocentric latitude and longitude used as seed values. The second Figure (5.5) plots the altitude of the seed points.

The results of the regularization procedure are shown in Figures 5.6, 5.7, and 5.8. A 500,000-generation-per-altitude genetic algorithm run was used to generate these profiles. In the case of this run, the starting position of the TMA points was not allowed to vary. Figures 5.6 and 5.7 show the zonal (east-west) and meridional (north-

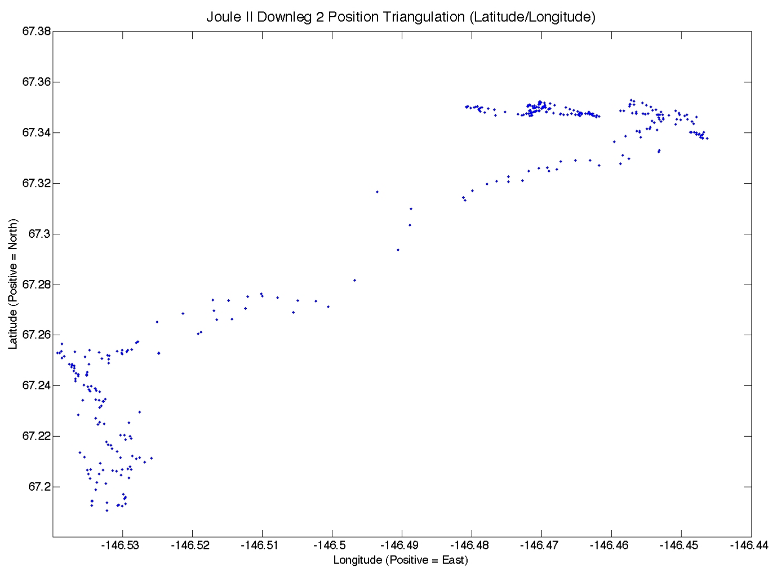

Figure 5.4: Joule II Downleg 2 Position Triangulation (Latitude and Longitude)

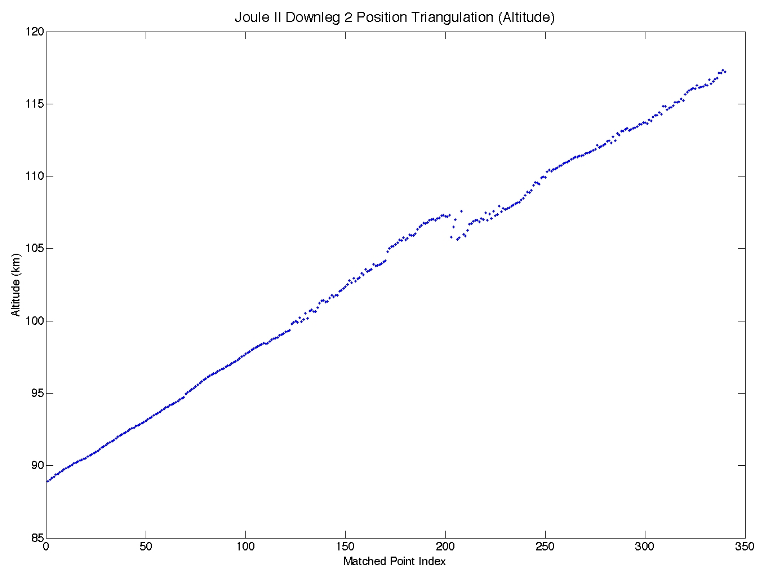

Figure 5.5: Joule II Downleg 2 Position Triangulation (Altitude)

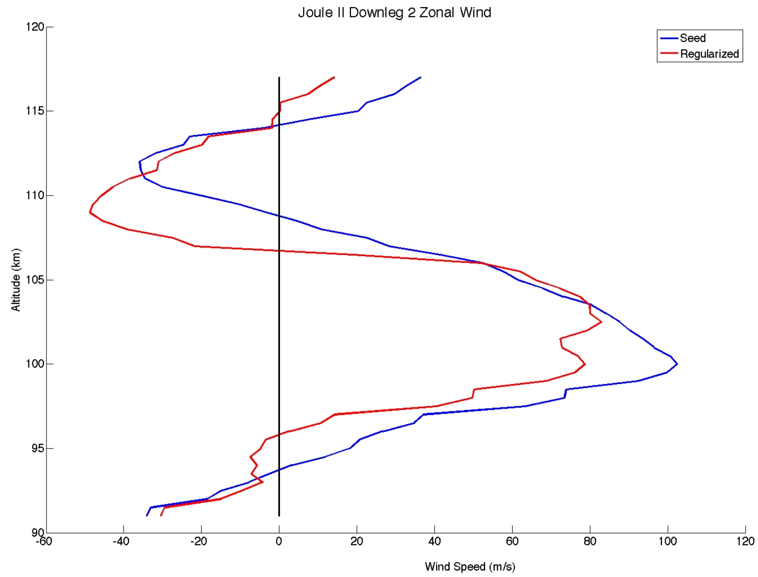

Figure 5.6: Joule II Downleg 2 Zonal Wind from Regularization

south) components of the wind. Positive velocities are eastward and northward, respectively. Figure 5.8 is a plot of wind magnitude versus altitude.

Figure 5.9 plots the average error at each altitude. Error is measured in pixels and is the distance from the calculated and projected wind point to the detected TMA points on the trail. The distance at each altitude is calculated for each image and averaged to produce this error metric.

Finally, Figures 5.10 and 5.11 show a representative set of the images used from Poker Flat and Fort Yukon, respectively. Plotted on the image are the projected TMA positions at the time the image was taken.

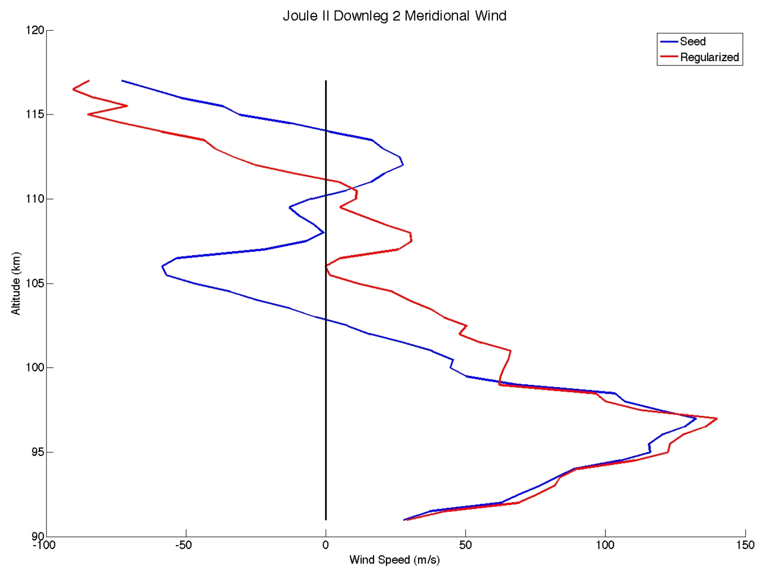

Figure 5.7: Joule II Downleg 2 Meridional Wind from Regularization

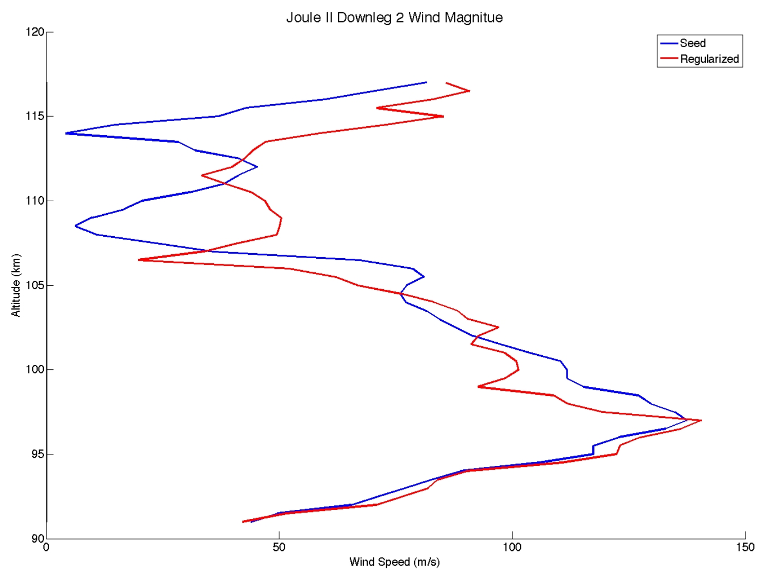

Figure 5.8: Joule II Downleg 2 Neutral Wind Magnitude from Regularization

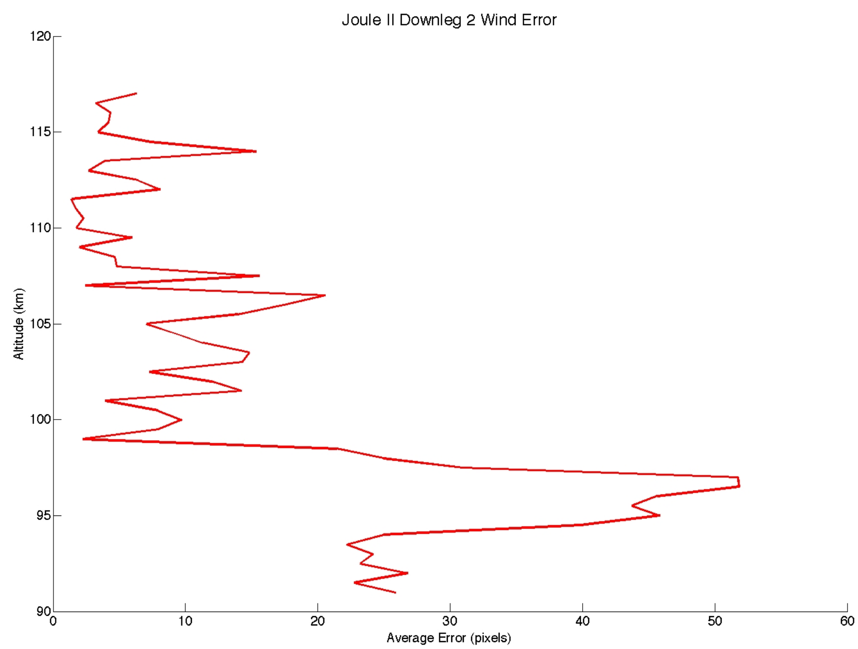

Figure 5.9: Joule II Downleg 2 Regularization Error

Figure 5.10: Joule II Downleg 2 Images from Poker Flat, AK

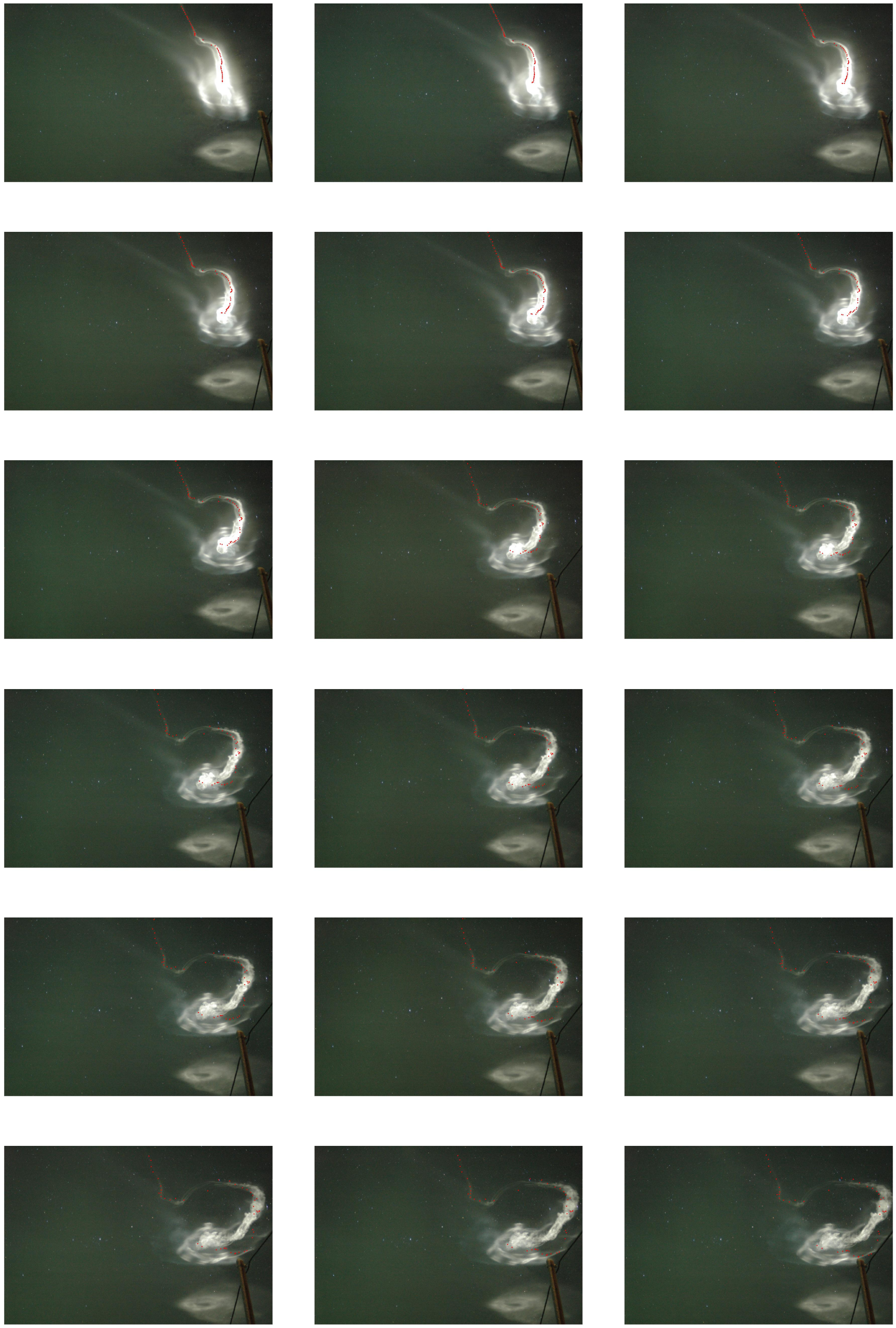

Figure 5.11: Joule II Downleg 2 Images from Fort Yukon, AK

5.2 HEX II

The second Horizontal E-region Experiment (HEX II) observed the vertical neutral winds in the E-region of the ionosphere. HEX II used four sounding rockets, three Terrier-Improved Orion rockets (vertical trajectory releases) and one Black Brant X (horizontal trajectory release). All rockets carried cold-cathode ionization gauges in addition to TMA. The three vertical rockets flew standard TMA release profiles and produced the typical upleg and downleg trails. The horizontal rocket, however, flew a tailored trajectory that allowed a horizontal release of TMA. The first two stages of the Black Brant X were used to loft the third stage and payload to the desired altitude. Upon reaching this altitude, the ACS (attitude control system) was used to reorient the rocket to a near-horizontal position. The final stage was then fired, imparting significant horizontal velocity. This allowed for a near-horizontal release of TMA, which was used to study the vertical component of the neutral wind.

5.2.1 Upleg 1

The upleg release from the first vertical rocket was selected for study due to the availability of digital images from all three camera sites. In addition, the PFISR (Poker Flat Incoherent Scatter Radar) was used to indirectly measure neutral winds. There are no seed wind values available for this release. Figures 5.12 and 5.13 (latitude/longitude and altitude, respectively) show the result of the automatic triangulation used to determine seed location. There are breaks in the seed values due to the spacing of the TMA puffs at high altitudes. Of the approximately 40 images available at each camera site, 12 from Fort Yukon and 8 from Coldfoot were used in the analysis.

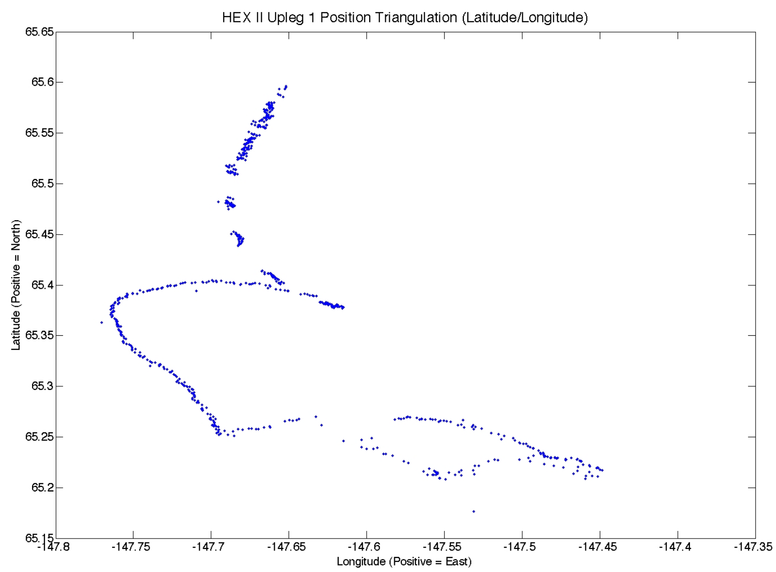

Figure 5.12: HEX II Upleg 1 Position Triangulation (Latitude/Longitude)

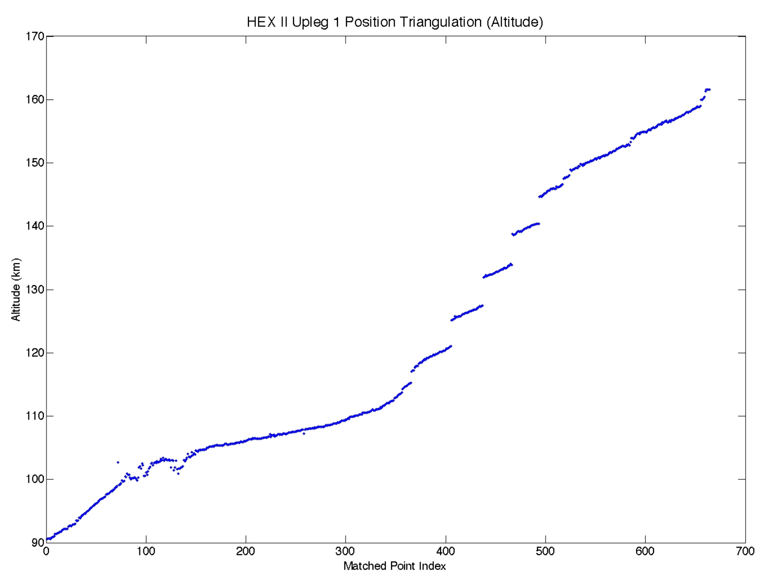

Figure 5.13: HEX II Upleg 1 Position Triangulation (Altitude)

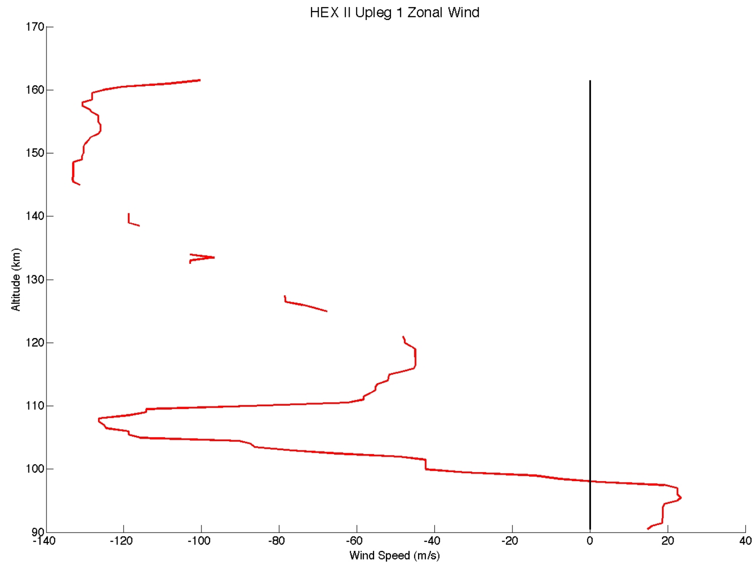

Figure 5.14: HEX II Upleg 1 Zonal Wind from Regularization

Figures 5.14 and 5.15 show the zonal and meridional neutral winds, respectively, determined using the regularization procedure. These profiles were generated from a 50,000-generation-per-altitude genetic algorithm run. As there are no seed winds available, the seed wind was set to 0 at all altitudes. As with the Joule II downleg results, the starting position was not permitted to vary for this regularization run. The breaks in the seed position values result in corresponding breaks in the wind profiles. It is not possible to estimate wind at these altitudes without extremely large errors. Figure 5.17 plots average pixel error as a function of altitude in the same manner as the error plot for the Joule II results.

Figures 5.18 and 5.19 show all of the images used to determine the neutral wind profiles for HEX II. The figures show images from Fort Yukon and Coldfoot, respectively.

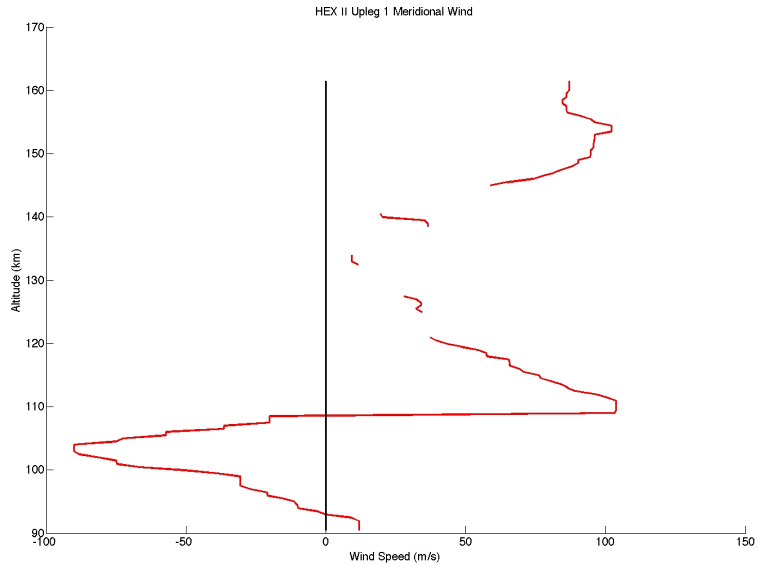

Figure 5.15: HEX II Upleg 1 Meridional Wind from Regularization

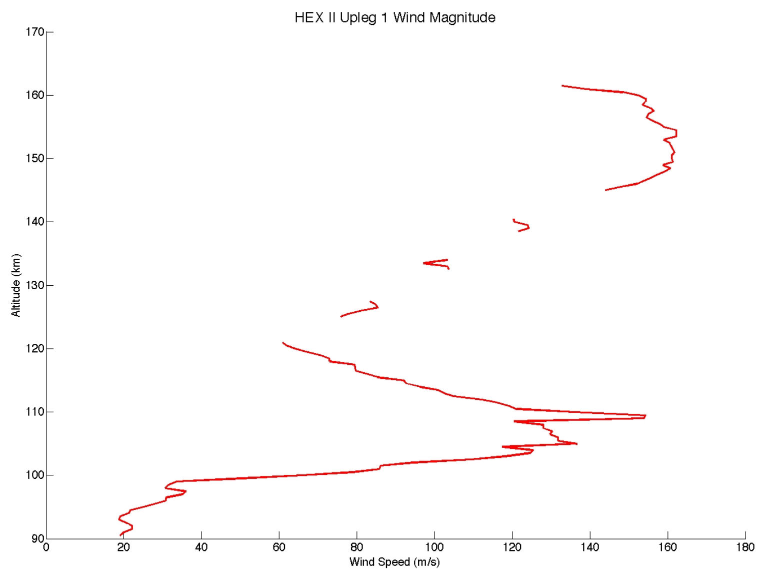

Figure 5.16: HEX II Upleg 1 Neutral Wind Magnitude from Regularization

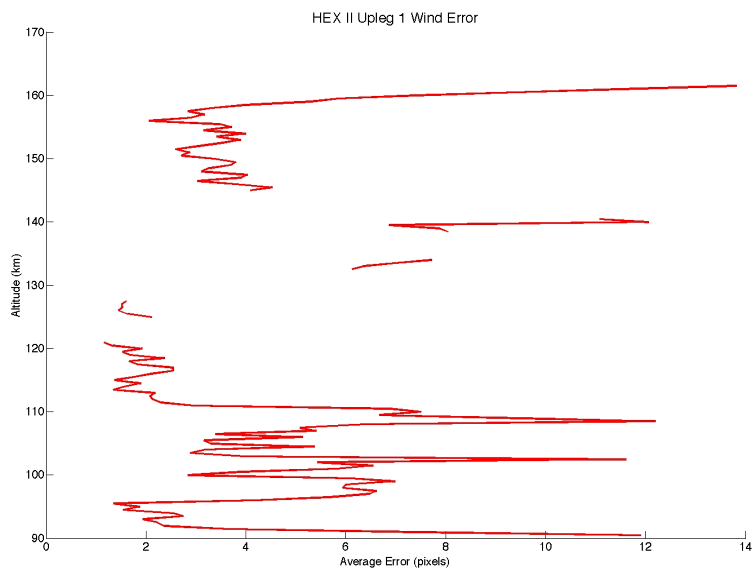

Figure 5.17: HEX II Upleg 1 Regularization Error

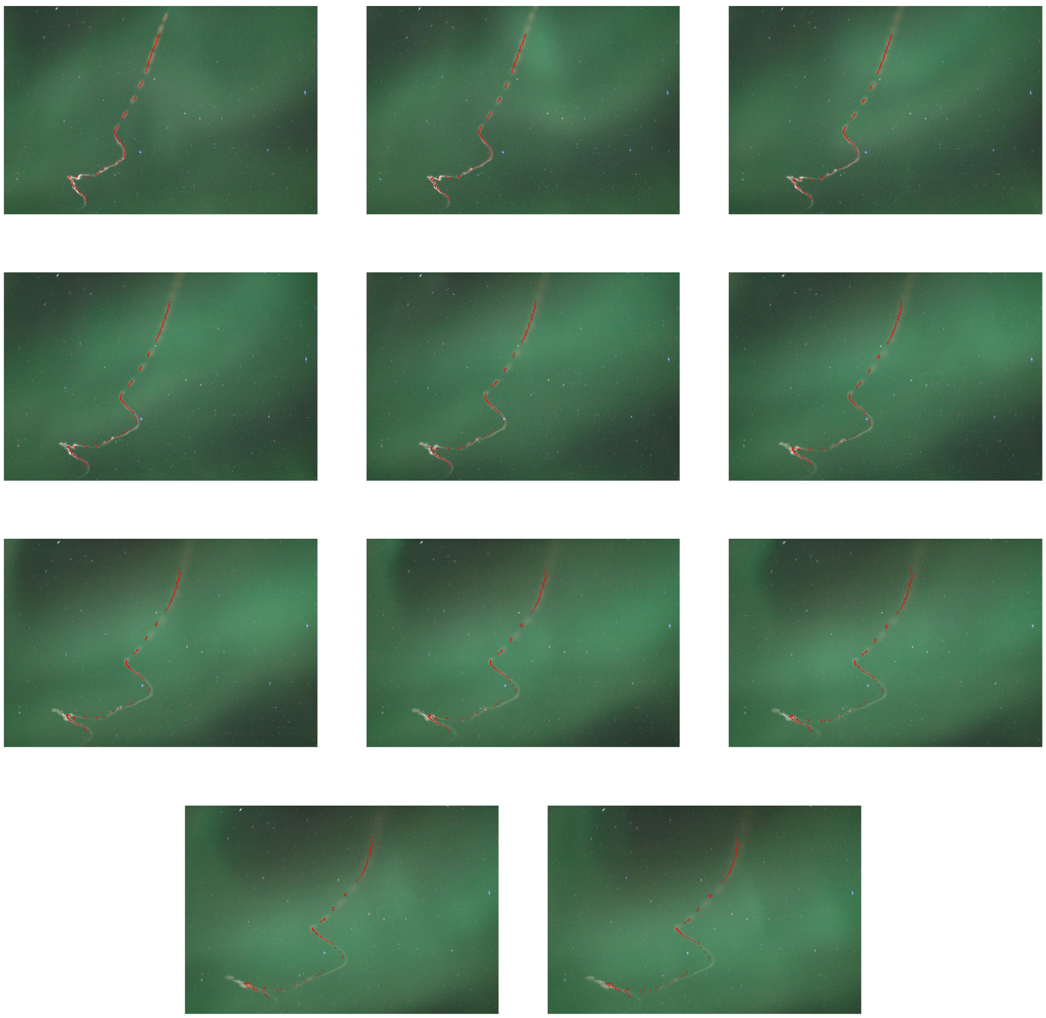

Figure 5.18: HEX II Upleg 1 Images from Fort Yukon, AK

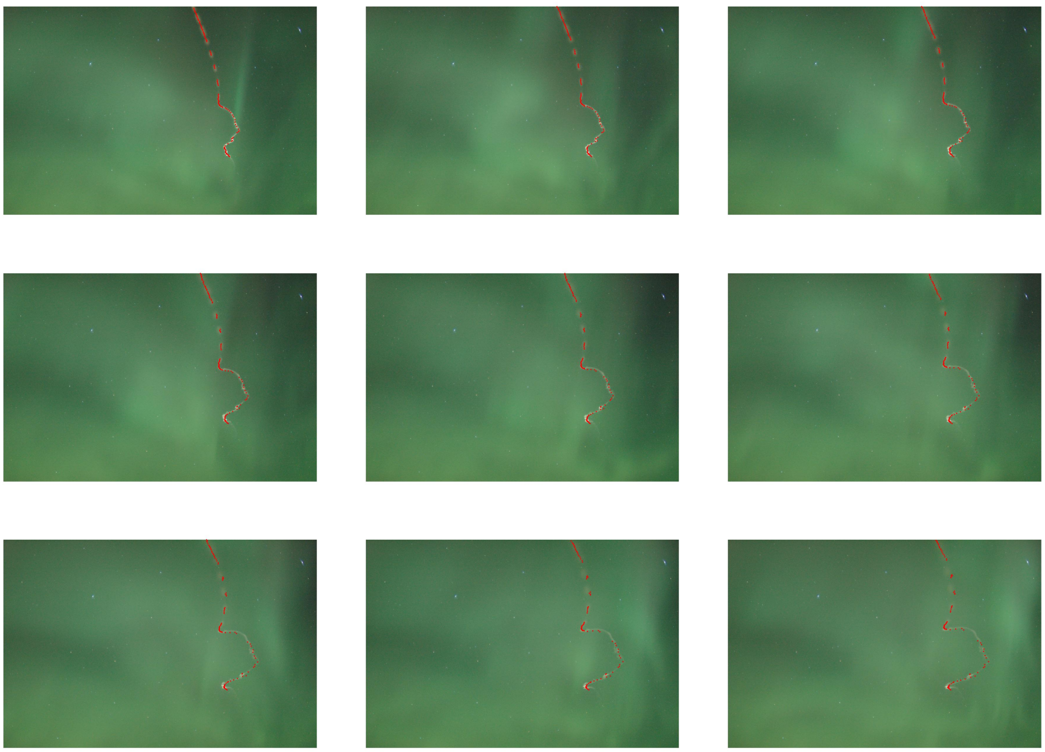

Figure 5.19: HEX II Upleg 1 Images from Coldfoot, AK

Chapter 6

Conclusions and Discussion

6.1 Joule II Downleg 2 Analysis

The images of the second Joule II downleg release are dirtier than most for the automatic detection of TMA. Figure 6.1 shows two representative images taken from Fort Yukon, Alaska with the detected TMA points plotted in red. In addition to the TMA trail begin analyzed, the image contains the remains of another upleg trail and a utility pole. In addition to these features, the trail is relatively close to the camera so much detail is visible in the lower portion of the trail. The turbulent mixing that occurs below the turbopause has resulted in a TMA trail that is very nonuniform in color and brightness in the first image. This roughness is reduced, in part, by the median filter used to smooth the image, but the lower portion of the trail still has the noisiest line of detected TMA points due to these properties. The upper portions, however, allow for a much smoother line of detected points.

The second image, however, has the opposite problem in the lower portion of the trail. The TMA is so bright that it saturated the detector in the camera and resulted in an area of pure white pixels. This may overpower any actual structure in the trail in this region and reduce the TMA pixel detection to finding the center of the bright region, which is not ideal. Finally, both images show only a portion of the trail, which prevents analysis of the entire downleg trail.

The seed winds and those calculated from the regularization procedure are plotted on the same axes in Figure 6.2. The red lines are the winds produced from regularization while the blue lines come from the seed values (which were determined using the traditional triangulation algorithm). The solid lines are the zonal winds, and the meridional line are indicated with dashed lines.

In examining the zonal winds (solid lines), there is much similarity. The winds peak at slightly different altitudes – 105 and 109 kilometers versus 100 and 112 kilometers – but follow the same general trend of eastward, turning westward, and finally back toward east again. However, the peak amplitudes differ by 15 to 20 meters per second.

The meridional winds, however, do not match up as well as the zonal winds. There is a great deal of similarity below about 97 kilometers, but the two profiles then begin to diverge above that altitude. The same general trends in shape occur, but magnitudes are very different. The second wind peak at approximately 106 kilometers differs by 50 meters per second and the trend to the south at high altitudes begins several kilometers lower in the regularization-produced winds.

The better agreement in the east-west direction versus the north-south direction is a result of the geometry of the camera sites. The cameras at Poker Flat and Fort Yukon are both pointed approximately northward since the trail was located between the two sites in longitude but north of both in latitude. This results in both cameras

Figure 6.1: Representative Joule 2 Downleg 2 Images for TMA Detection

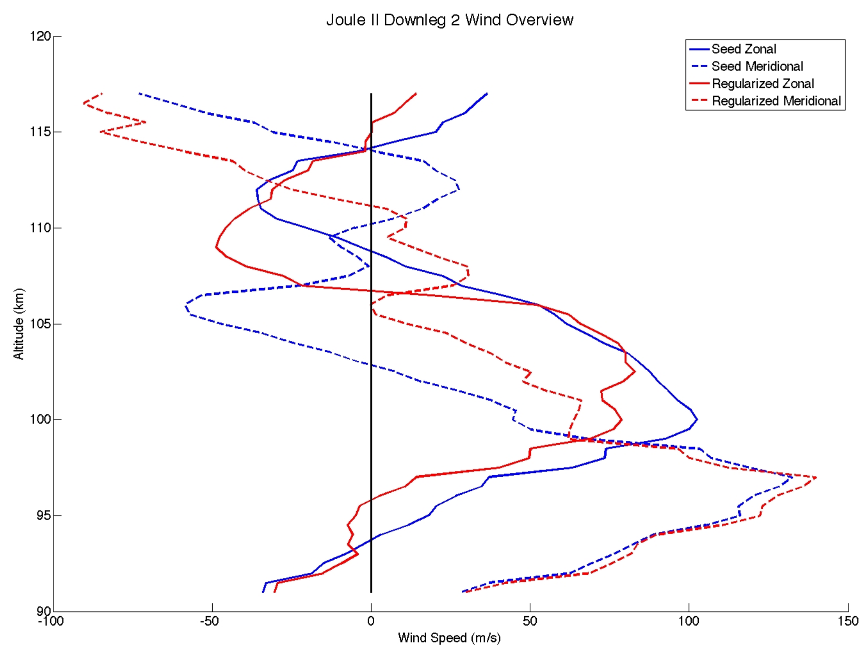

Figure 6.2: Joule II Downleg 2 Neutral Wind Components from Regularization

seeing similar trails, offset by only a few degrees in azimuth. The similar viewpoints lead to good measurements of zonal winds as movements in the zonal direction show up as horizontal motions in both cameras. Movement in the meridional direction, however, results in movement towards or away from the cameras, which is more difficult to detect.

After analysis, the regularization results for the second Joule II downleg are slightly more believable than the results from traditional triangulation. The zonal winds show good agreement and the peculiarities of the camera viewpoints make absolute statements about the meridional winds difficult. Figure 6.3 shows the pixel errors for the regularization-derived winds in blue and the errors for the winds from the traditional triangulation in red. The errors for the traditional triangulation were calculated in the same manner as the the regularization errors. The lower altitudes (below 97 kilometers) show similar error values, which is expected since the two methods showed a high level of agreement in that range. Altitudes above 97 kilometers show significantly smaller errors for the regularization-based winds. This improvement in error values implies that the regularization procedure is an improvement over the traditional triangulation technique.

As far as the performance of the regularization algorithm itself is concerned, the results for this trail are good but not great. As is evident in the error plot and sample images (Figures 5.9, 5.10, and 5.11), the chosen winds miss by several tens of pixels at certain altitudes in later images. This is partially due to the above limitations in the viewing geometry, but may also have been mitigated if the starting positions were allowed to change from the seed positions during processing.

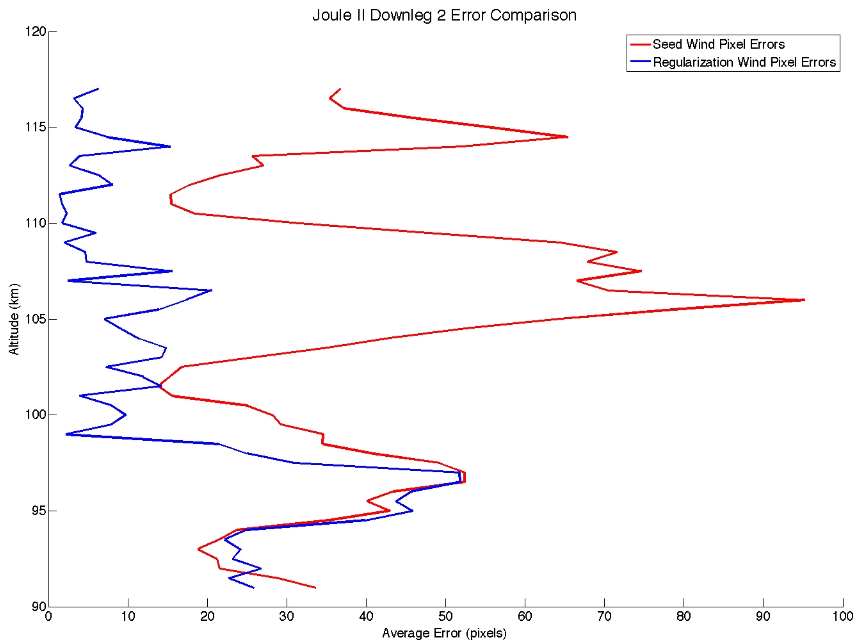

Figure 6.3: Joule II Downleg 2 Pixel Error Comparison

Finally, returning to Figure 6.2, where the meridional and zonal winds are plotted on the same axes, both the seed and regularized values show an approximately 180 degree phase difference. As the zonal wind increases, the meridional wind tends to decrease. Both the blue curves (seed wind) and red curves (regularized wind) show this feature, which is present on many wind profiles from this region.

6.2 HEX II Upleg 1 Analysis

The images of the first upleg release from HEX II are much better suited to the detection of TMA when compared to the Joule II second downleg images. Two representative images, are shown in Figure 6.4, with the detected TMA points plotted in red. The trails are farther away from the camera sites and the majority of the release is visible. In addition, the rough nature of the lower portions of the trail does not affect the TMA detection process as much since the trail is smaller in the field of view of the camera.

Both images show good detection of TMA, with the gaps between the upper-altitude TMA puffs visible and the sharp angles in the lower portions of the trail detected. The upper image is from Coldfoot, Alaska and does show two artifacts where stars were detected as TMA. A few outlier pixels like these do not affect the regularization process and do not need to be removed. The lower image is from Fort Yukon, Alaska and also shows a few artifacts and a gap in the trail where there should be visible TMA. The TMA in that section had faded too much to be detected. Again, these problems in TMA detection do no affect the final wind profiles.

In this case, the viewing geometry is more suited to good determination of both zonal and meridional winds. Since the trail is in the vicinity of Poker Flat, the

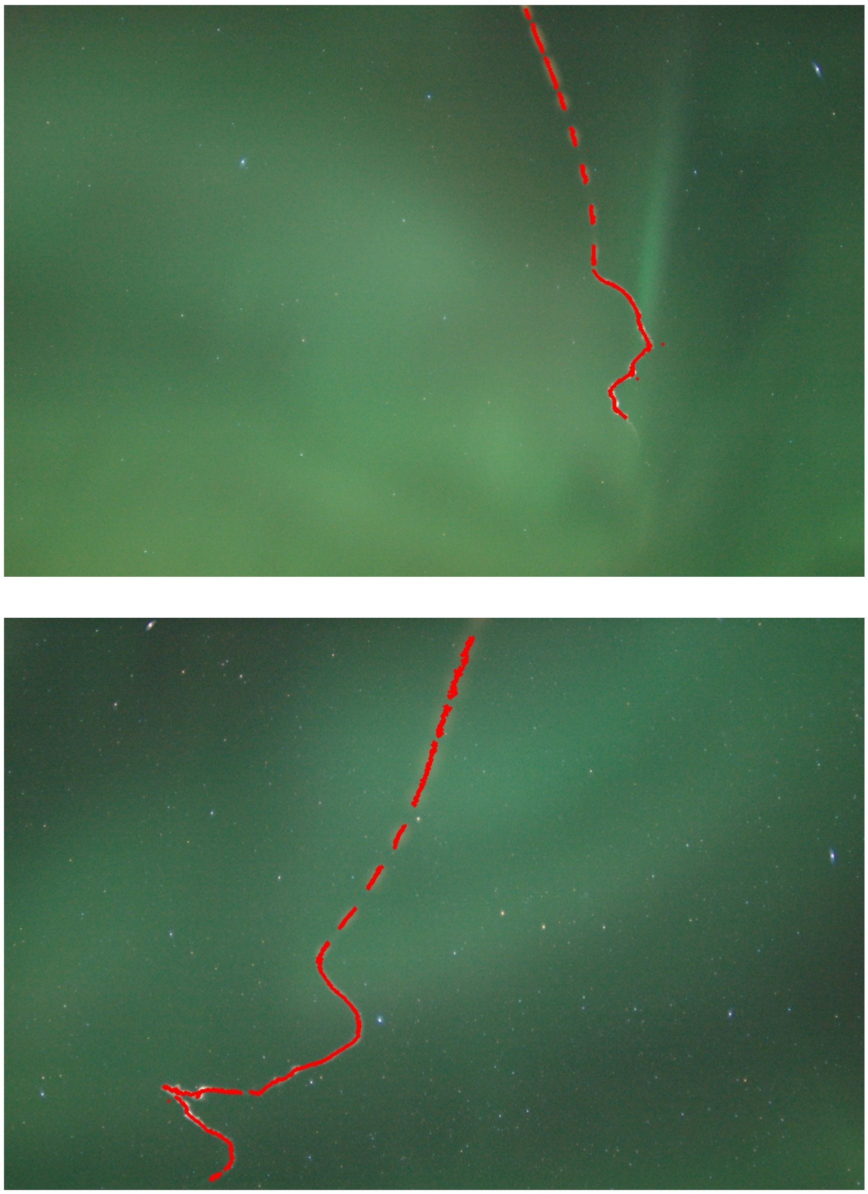

Figure 6.4: Representative HEX II Upleg 1 Images for TMA Detection

cameras at Fort Yukon and Coldfoot were looking back toward the launch site. The cameras observed both sides of the trail from azimuths that were sufficiently different to make north-south, as well as east-west movements discernible.

A triangulation was performed for this trail by Wescott [20], but only for altitudes in the 110 to 180 kilometer range. Figure 6.5 shows the zonal and meridional winds plotted on the same axes. The blue curves are the winds from the Wescott triangulation (zonal solid and meridional dashed), and the red curves are the winds from the regularization procedure (zonal solid and meridional dashed). The two zonal profiles match almost perfectly throughout the entire range of overlapping altitudes (115 to 160 kilometers). The meridional profiles, however, only agree from 115 through 130 kilometers and from 150 to 160 kilometers. The altitude range in between shows a large disagreement, which may be caused by the sparse nature of the trail at these altitudes due to the puffing of the release. Though it is more visible in the lower portion of the trial, the entire altitude range shows the same approximate 180 degree phase difference also shown by the Joule II second downleg. In addition, the gaps in the data due to the spaces between the TMA puffs follow the general trend of the profile surrounding them.

Convergence for this trail was much faster than for the Joule II trail, 50,000 versus 500,000 generations. As in the Joule II trail, the starting positions of the HEX II first upleg TMA trail were fixed to the seed positions. Unlike the other trail, seed winds were not available as the Wescott winds were too sparse and only covered a subset of the visible range. As a result, the search procedure was nominally more difficult since the starting winds were arbitrarily set to zero.

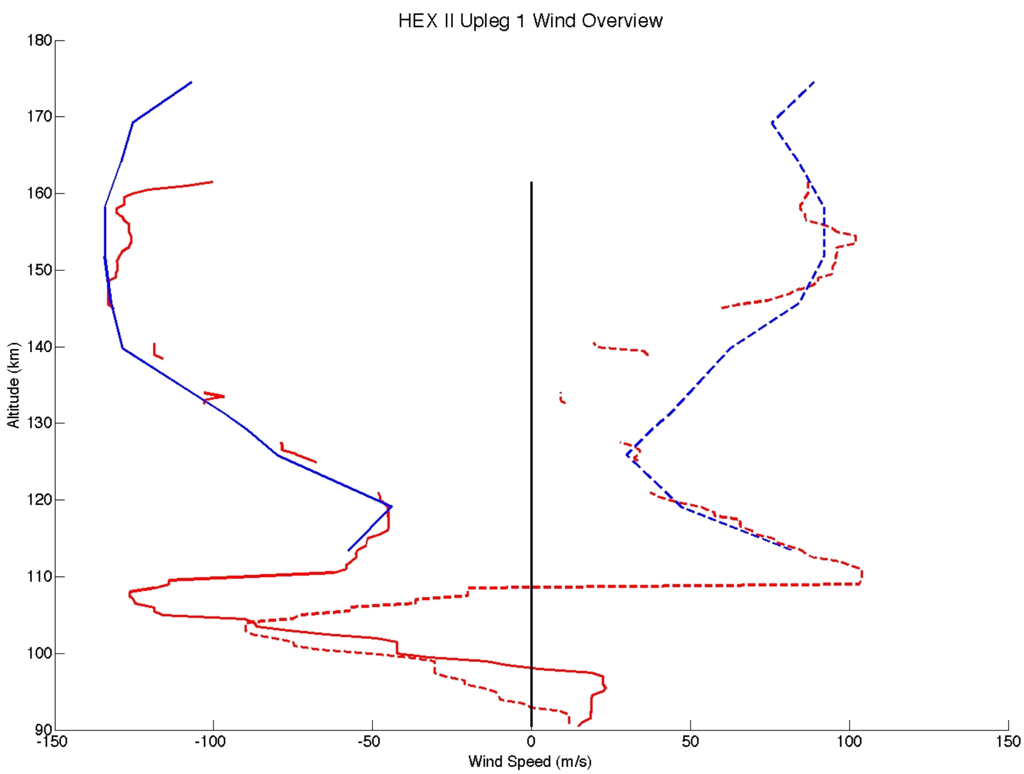

Figure 6.5: HEX II Upleg 1 Neutral Winds

In general, the regularization algorithm performed very well on this trail. As the images in Figures 5.18 and 5.19 show, the projection of TMA positions at different times agree very well with the trails themselves. This is reflected in the average pixel error plot, which is less than fifteen pixels for all altitudes.

6.3 Regularization Algorithm

In general, the automated, regularization-based approach to neutral wind determination is well-suited to the overall problem. The TMA trails both showed good to excellent results and were taken from different camera configurations and rocket motions (upleg versus downleg). The common 180 degree phase offset was seen in both profiles and the one profile with comparison data available for comparison agreed reasonably well.

6.4 Future Work

The most beneficial addition to the regularization procedure for wind determination would be a method that allows the starting positions to change from the seed positions during the genetic algorithm-based search. As currently implemented, allowing these two extra degrees of freedom lets the algorithm converge into a state where pixels from different altitude bins congregate in a few areas along the trail, which results in spurious wind values.

Convergence speed can also be improved. As generation counts of 50,000 to 500,000 are required for quality results in the current algorithm, any increase in computational efficiency or speed is significant. Porting the entire procedure to C or using one of the commercially available MATLAB compilers may provide some speedup. In addition, simulated annealing-based algorithms may converge faster in some circumstances, so an investigation of using simulated annealing instead of a genetic algorithm in the search procedure may also be a source for improved performance. [11]

Changes in the algorithm to better deal with the appearance or disappearance of trail points would improve accuracy, as would better handling of the gaps in the seed winds and position profiles that occur where discrete puffs are visible. Finally, both the Joule II and HEX II trails were processed using digital camera images. Use of Hasselblad or film Nikon images, possibly mixed in with the digital images may also provide increased accuracy.

6.5 Final Thoughts

The determination of neutral wind velocity from photographs of sounding rocket chemical releases is a nontrivial problem. The algorithms developed in this thesis attempt to add a degree of automation to the procedure. In addition, the restriction on processing pairs of simultaneous images has been reduced to simply requiring one pair of near-simultaneous images for the calculation of seed positions. Comparison of regularization results with the Joule II traditional triangulation winds shows an improvement in error, and the HEX II results agreed remarkably well with the available data from Wescott.

Appendices

Appendix A Date and Time Systems

A.1 Julian Date

The Julian date system is a simple calendar based on the number of days (and fractions of days) that have elapsed since noon on January 1, 4713 BCE. This calendar is particularly suited to astronomy since it starts at noon, thus placing an entire night's observations in the same day for most longitudes. In addition, the simple count of days avoids complexities such as leap years and the differing lengths of months. [15]

A.2 Coordinated Universal Time

Coordinated universal time, also know at UTC, is derived from the rotation of the earth. Specifically, it tracks the position of the sun as seen from the prime meridian ($0°$ longitude). In essence, it is the time of day on the prime meridian. [3]

A.3 Sidereal Time

Julian dates, as well as most other calendar and time systems, are based on the solar day. Sidereal time, however, is based on the motion of the stars in the sky. The sidereal day is approximately 4 minutes shorter than the solar day, which is solely based on the rotation of the Earth. The sidereal day also takes into account the progress of the Earth along its orbit. This additional factor essentially shortens the sidereal day with respect to the solar day. [15]

Sidereal time has concepts corresponding to the local time and universal time used with the solar day. The equivalent terms are local sidereal time (Θ) and Greenwich mean sidereal time (Θ_0), respectively. Greenwich mean sidereal time can be calculated from the corresponding Julian date, after which, local sidereal time can be calculated from the observer's longitude (λ). Fifteen degrees of longitude are equivalent to one hour of displacement in sidereal time. [15]

$$\Theta = \Theta_0 + \frac{\lambda}{15} \tag{1}$$

Appendix B Coordinate Systems

B.1 Equatorial

The equatorial coordinate system has two components, right ascension (α) and declination (δ). Equatorial coordinates are measured with respect to the equatorial plane, which passes through the equator and thus is perpendicular to the axis of rotation. [15] Declination is analogous to latitude in the geographic coordinate system and is a measure of the angle between the equatorial plane and an arbitrary point on the celestial sphere. Likewise, right ascension is analogous to longitude and is the angular distance between a point in the sky and the first point in Aries. Also known as the vernal equinox point, the first point in Aries is where the sun crosses the celestial equator at the March equinox. Declination is measured in degrees and right ascension is measured in hours – there are 24 hours in a complete circle.

There is an additional coordinate used with the equatorial system. The hour angle (τ) is a measure of the time since a point in the sky has crossed the meridian. Thus, a point with hour angle of 0 is directly on the meridian. Hour angle is measured in hours in the same manner as right ascension. The hour angle of a point can be determined from the local sidereal time (Θ) and the right ascension of the point using the formula [15]

$$\tau = \Theta - \alpha \tag{2}$$

B.2 Standard

The standard coordinate system (X, Y) places an imaginary plane tangent to the celestial sphere and projects star positions from the sphere onto that plane. Standard coordinates are desirable for astrometric processing because the projection onto a plane is very similar to the formation of an image in a telescope. Standard coordinates are unitless.[1]

B.3 Plate

Plate coordinates (x, y), also known as image coordinates, are used to specify a specific location in a photograph or other image of the sky. x and y are cartesian coordinates, though two different origins are commonly used. Image processing traditionally places the origin in the upper left with the x-axis positive to the right and the y-axis positive down. Other fields place the origin at the center of the picture with the x-axis positive to the right and the y-axis positive up.

In the case of digital images or scanned negatives, the plate coordinates of an arbitrary pixel can be determined from knowledge of the camera's frame size and the resolution of the digital image. Plate coordinates are measured in pixels or milimeters.

B.4 Horizontal

The horizontal coordinate system, also known as the horizon system, consists of azimuth and elevation. Azimuth (A) is the measurement of the angular displacement (eastward positive) from true north. Azimuth is sometimes measured from south, westward positive, but not in this case. Elevation (h), also called altitude, is the measure of the angle between the horizon and a point in the sky. Thus, any point on the horizon is at $0°$ elevation and the zenith point is at $90°$ elevation. This coordinate system is not suited to all astronomy applications due to its dependence on the observer's latitude. [15]

B.5 Geographic

The geographic coordinate system consists of the familiar latitude (ϕ) and longitude (λ), as well as elevation above sea level. Latitude is $0°$ at the equator, $90°$ at the north pole, and $-90°$ at the south pole. Longitude is $0°$ on the prime meridian and positive eastward. As a result, longitude in the western hemisphere is negative.

In some circumstances, geocentric latitude (ϕ') may be more useful than the standard geographic latitude. Geocentric latitude takes into account the fact that the Earth is not perfectly spherical, but can be approximated as a perfect ellipsoid of revolution about the rotation axis. The equatorial radius (a) is approximately 6378.099 km and the polar radius (b) is about 6356.631 km. This leads to the following correction for latitude (3), but not longitude, due to the assumption that the Earth is a surface of revolution [14].

$$\phi' = \tan^{-1}\left(\frac{b^2}{a^2}\tan\phi\right) \tag{3}$$

The assumed ellipsoid of revolution also requires a correction to the radial distance from the center of the Earth to a point on the surface, depending on geocentric latitude. The total radial distance to a point is $R' = R + H$ where H is the altitude above sea level and R is determined from (4)

$$R = \frac{b}{\left[1 - \left(1 - \frac{b^2}{a^2}\right)\cos^2\phi'\right]^{1/2}} \tag{4}$$

B.6 Geocentric

The geocentric coordinate system defines a set of right-handed Cartesian axes located at the center of the Earth. The x-axis points to the intersection of the prime meridian with the equator. The y-axis is directed at the intersection of the 90° east meridian with the equator, and the z-axis points toward the north pole.

B.7 Topocentric

The topocentric coordinate system defines a set of right-handed Cartesian axes located at a point on the Earth's surface. The x-axis is vertical, along the line from the center of the earth to the point. The y-axis points due east of the point, orthogonal to the x-axis, and the z-axis points north from the point, again orthogonal to the x-axis.

Appendix C Coordinate System Conversions

C.1 Equatorial to Standard

(α, δ) are equatorial coordinates of the star while (α_0, δ_0) are the equatorial coordinates of the center of the image or starfield, and (X, Y) are the corresponding standard coordinates given by [15].

$$
\begin{aligned}
X &= -\frac{\cos(\delta)\sin(\alpha-\alpha_0)}{cos(\delta_0)\cos(\delta)\cos(\alpha-\alpha_0)+\sin(\delta_0)\sin(\delta)} \\
Y &= -\frac{\sin(\delta_0)\cos(\delta)\cos(\alpha-\alpha 0)-\cos(\delta_0)\sin(\delta)}{\cos(\delta_0)\cos(\delta)\cos(\alpha-\alpha_0)+\sin(\delta_0)\sin(\delta)}
\end{aligned} \tag{5}
$$

C.2 Standard to Equatorial

(X, Y) are the standard coordinates of the point, (α_0, δ_0) are the equatorial coordinates of the center of image, and (α, δ) are the corresponding equatorial coordinates given by [15]

$$
\begin{aligned}
\alpha &= \alpha_0 + \arctan\left(\frac{-X}{\cos(\delta_0) - Y\sin(\delta_0)}\right) \\
\delta &= \arcsin\left(\frac{\sin(\delta_0) + Y\cos(\delta_0)}{\sqrt{1+X^2+Y^2}}\right)
\end{aligned} \tag{6}
$$

C.3 Horizontal to Equatorial

This conversion is used to determine the center – in equatorial coordinates – of the photographs of the TMA trails. The approximate azimuth and elevation of the camera are known because these are set prior to launch to ensure that the desired TMA trail is in the camera's field of view. Here (A, h) are the horizontal coordinates of the camera pointing, ϕ is latitude, and (δ, τ) are the corresponding declination and hour angle. [3] Right ascension can be determined from hour angle by (2). The conversion is given by

$$\begin{aligned} \delta &= \arcsin(\sin(h)\sin(\phi) + \cos(h)\cos(\phi)\cos(A)) \\ \tau &= \arccos\left(\frac{\sin(h) - \sin(\phi)\sin(\delta)}{\cos(\phi)\cos(\delta)}\right) \end{aligned} \tag{7}$$

A correction to the calculated value for τ may be required due to the range of the inverse cosine function. If $\sin(A)$ is negative, then the calculated τ is the true azimuth. Otherwise, the hour angle is actually $360 - \tau$. [3]

C.4 Equatorial to Horizontal

(δ, τ) are the declination and hour angle of the point, ϕ is the latitude of the observation, and (A, h) are the corresponding horizontal coordinates. [3] The conversion is given by

$$\begin{aligned} h &= \arcsin(\sin(\delta)\sin(\phi) + \cos(\delta)\cos(\phi)\cos(\tau)) \\ A &= \arccos\left(\frac{\sin(\delta) - \sin(\phi)\sin(h)}{\cos(\phi)\cos(h)}\right) \end{aligned} \tag{8}$$

A correction to the calculated value for A may be required due to the range of the inverse cosine function. If $\sin(\tau)$ is negative, then the calculated A is the true azimuth, otherwise, the azimuth is actually $360 - A$. [3]

C.5 Geographic to Geocentric

If R' is the radial distance from the center of the Earth to the point in question, ϕ' is the geocentric latitude, and θ is longitude, the conversion is given by

$$\begin{aligned} x &= R' \cos\phi' \cos\theta \\ y &= R' \cos\phi' \sin\theta \\ z &= R' \sin\phi' \end{aligned} \tag{9}$$

C.6 Topocentric to Geocentric

(x_G, y_G, z_G) are coordinates in the geocentric system while (x_T, y_T, z_T) are the corresponding coordinates in the topocentric system. ϕ is geocentric latitude and θ is longitude. The relevant expressions can be written in matrix form as

$$\begin{bmatrix} x_T & y_T & z_T \end{bmatrix} \begin{bmatrix} \cos\theta\cos\phi & \sin\theta\cos\phi & \sin\phi \\ -\sin\theta & \cos\theta & 0 \\ -\cos\theta\sin\phi & -\sin\theta\sin\phi & \cos\phi \end{bmatrix} = \begin{bmatrix} x_G & y_G & z_G \end{bmatrix} \tag{10}$$

C.7 Geocentric to Topocentric

(x_G, y_G, z_G) are coordinates in the geocentric system while (x_T, y_T, z_T) are the corresponding coordinates in the topocentric system. ϕ is geocentric latitude and θ is longitude. Note that this is the transpose of the topocentric to geocentric conversion and is given by

$$\begin{bmatrix} x_G & y_G & z_G \end{bmatrix} \begin{bmatrix} \cos\theta\cos\phi & \sin\theta\cos\phi & \sin\phi \\ -\sin\theta & \cos\theta & 0 \\ -\cos\theta\sin\phi & -\sin\theta\sin\phi & \cos\phi \end{bmatrix}^{\mathrm{T}} = \begin{bmatrix} x_T & y_T & z_T \end{bmatrix} \tag{11}$$

Appendix D Closest Approach of Two Vectors

The closest approach of two vectors is calculated during both the manual and automatic triangulation procedures.

D.1 Input Variables and Equations

In the following expressions $\boldsymbol{R_A}$ and $\boldsymbol{R_B}$ are the locations of sites A and B in geocentric coordinates, while $\hat{e_A}$ and $\hat{e_B}$ are the geocentric target vectors from sites A and B for the chosen pair of corresponding points

$$
\begin{aligned}
\boldsymbol{R_A} &= [x_A \quad y_A \quad z_A]^{\mathrm{T}} \\
\boldsymbol{R_B} &= [x_A \quad y_B \quad z_B]^{\mathrm{T}} \\
\hat{\boldsymbol{e_A}} &= [e_{Ax} \quad e_{Ay} \quad e_{Az}]^{\mathrm{T}} \\
\hat{\boldsymbol{e_B}} &= [e_{Bx} \quad e_{By} \quad e_{Bz}]^{\mathrm{T}}
\end{aligned}
\tag{12}
$$

The distance between two points on the lines leaving the camera sites in the direction of the target vectors is given by

$$
\begin{aligned}
D^2 = &[(Ae_{Ax} + x_A) - (Be_{Bx} + x_B)]^2 + \\
&[(Ae_{Ay} + y_A) - (Be_{By} + y_B)]^2 + \\
&[(Ae_{Az} + z_A) - (Be_{Bz} + z_B)]^2
\end{aligned}
\tag{13}
$$

The location points on the lines are determined by A and B, which scale $\hat{e_A}$ and $\hat{e_B}$.

D.2 Minimization of (13)

Taking the partial derivatives of (13) with respect to A and B.

$$\begin{aligned}\frac{\partial}{\partial A} D^2 =& 2e_{Ax}\left[(Ae_{Ax} + x_A) - (Be_{Bx} + x_B)\right] + \\ & 2e_{Ay}\left[(Ae_{Ay} + y_A) - (Be_{By} + y_B)\right] + \\ & 2e_{Az}\left[(Ae_{Az} + z_A) - (Be_{Bz} + z_B)\right] \\ & = A\hat{\boldsymbol{e_A}} \cdot \hat{\boldsymbol{e_A}} - B\hat{\boldsymbol{e_A}} \cdot \hat{\boldsymbol{e_B}} \\ & = (\boldsymbol{R_A} - \boldsymbol{R_B}) \cdot \hat{\boldsymbol{e_A}}\end{aligned} \tag{14}$$

By symmetry:

$$\frac{\partial}{\partial B} D^2 = (\boldsymbol{R_B} - \boldsymbol{R_A}) \cdot \hat{\boldsymbol{e_B}} \tag{15}$$

D.3 Equivalent Matrix Formulation

We can write the expressions as

$$\begin{bmatrix} a_{11} & a_{12} \\ a_{21} & a_{22} \end{bmatrix} \begin{bmatrix} A \\ B \end{bmatrix} = \begin{bmatrix} c_1 \\ c_2 \end{bmatrix} \tag{16}$$

where

$$
\begin{aligned}
a_{11} &= \hat{\boldsymbol{e}_{\boldsymbol{A}}} \cdot \hat{\boldsymbol{e}_{\boldsymbol{A}}} \\
a_{12} &= -\hat{\boldsymbol{e}_{\boldsymbol{A}}} \cdot \hat{\boldsymbol{e}_{\boldsymbol{B}}} \\
a_{21} &= -\hat{\boldsymbol{e}_{\boldsymbol{A}}} \cdot \hat{\boldsymbol{e}_{\boldsymbol{A}}} \\
a_{22} &= \hat{\boldsymbol{e}_{\boldsymbol{B}}} \cdot \hat{\boldsymbol{e}_{\boldsymbol{B}}} \\
c_1 &= (\boldsymbol{R_A} - \boldsymbol{R_B}) \cdot \hat{\boldsymbol{e}_{\boldsymbol{A}}} \\
c_2 &= (\boldsymbol{R_B} - \boldsymbol{R_A}) \cdot \hat{\boldsymbol{e}_{\boldsymbol{B}}}
\end{aligned} \tag{17}
$$

D.4 Solving for A and B

The solution is found by inverting the a_{ij} matrix and premultiplying the inverse to the left and right sides of the equation to get

$$
A = \frac{(\boldsymbol{R_B} - \boldsymbol{R_A})}{1 - (\hat{\boldsymbol{e}_{\boldsymbol{A}}} \cdot \hat{\boldsymbol{e}_{\boldsymbol{B}}})^2} \cdot [\hat{\boldsymbol{e}_{\boldsymbol{A}}} - (\hat{\boldsymbol{e}_{\boldsymbol{A}}} \cdot \hat{\boldsymbol{e}_{\boldsymbol{B}}})] \tag{18}
$$

$$
B = \frac{(\boldsymbol{R_B} - \boldsymbol{R_A})}{1 - (\hat{\boldsymbol{e}_{\boldsymbol{A}}} \cdot \hat{\boldsymbol{e}_{\boldsymbol{B}}})^2} \cdot [(\hat{\boldsymbol{e}_{\boldsymbol{A}}} \cdot \hat{\boldsymbol{e}_{\boldsymbol{B}}}) - \hat{\boldsymbol{e}_{\boldsymbol{B}}}] \tag{19}
$$

D.5 Result

The point halfway between the vectors at closest approach in geocentric coordinates and is the distance (in km) between the two vectors at closest approach are given by

$$
\boldsymbol{R} = \frac{1}{2}\left[\boldsymbol{R_A} + A\hat{\boldsymbol{e}_{\boldsymbol{A}}} + \boldsymbol{R_B} + B\hat{\boldsymbol{e}_{\boldsymbol{B}}}\right] \tag{20}
$$

$$\Delta S = \frac{1}{2} \left| \boldsymbol{R_B} + B\hat{\boldsymbol{e_B}} - (\boldsymbol{R_A} + A\hat{\boldsymbol{e_A}}) \right| \tag{21}$$

This is an error metric.

Bibliography

[1] Richard Berry and James Burnell. *The Handbook of Astronomical Image Processing*. Willmann-Bell, 2000.

[2] Fabien Chéreau and Matthew Gates. Stellarium, 2008.

[3] Peter Duffett-Smith. *Practical astronomy with your calculator*. Cambridge University Press, 1979.

[4] Geophysical Institute, University of Alaska Fairbanks. Poker flat research range, June 2008. Available from <http://http://www.pfrr.alaska.edu/>.

[5] R. I. Hartley and A. Zisserman. *Multiple View Geometry in Computer Vision*. Cambridge University Press, 2004.

[6] C Hermanson. Feasibility and design of a star-tracker attitude sensor system for sounding rocket flights. Master's thesis, Clemson Univeristy, 2005.

[7] John Houghton. The physics of atmospheres. Cambridge University Press, December 2001.

[8] Rudolph Emil Kalman. A new approach to linear filterming and prediction problems. *Transactions of the ASME–Journal of Basic Engineering*, 82(Series D):34–45, 1960.

[9] Michael Kass, Andrew Witkin, and Demitri Terzopoulos. Snakes: Active contour models. *International Journal of Computer Vision*, 1(4):321–331, 1988.

[10] Michael Kelley. *The Earth's Ionosphere, Plasma Physics and Electrodynamics*. Academic Press, 1989.

[11] S Kirkpatrick, C D Gelatt, and M P Vecchi. Optimization by simulated annealing. *Science*, (220):671–680, 1983.

[12] P. D. Kovesi. MATLAB and Octave functions for computer vision and image processing. School of Computer Science & Software Engineering, The University of Western Australia. Available from: <http://www.csse.uwa.edu.au/∼pk/research/matlabfns/>.

[13] M. F. Larsen, T. R. Marshal, I. S. Mikkelsen, B. A. Emery, A. Christensen, D. Kayser, J. Hecht, L. Lyons, and R. Walterscheid. Atmospheric response in aurora experiment: Observations of e and f region neutral winds in a region of postmidnight diffuse aurora. *Journal of Geophysical Research*, 100(A9):17299, 17308 1995.

[14] MF Larsen. Analysis techniques for determining upper atmosphere motions from sounding rocket chemical tracer releases. Private Correspondence, August 2004.

[15] Oliver Montenbruck and Thomas Pfleger. *Astronomy on the Personal Computer*. Springer-Verlag, 2002.

[16] Smithsonian Astrophysical Observatory. *Star catalog: Positions and Proper Motions of 258,997 Stars for the Epoch and Equinox of 1950.0*. Smithsonian Institution, 1971.

[17] Tom O'Haver. Peak finding and measurement. Technical report, University of Maryland at College Park, 2008.

[18] Robert W Schunk and Andrew F Nagy. *Ionospheres, Physics, Plasma Physics, and Chemistry*. Cambridge University Press, 2000.

[19] Luc Vincent and Pierre Soille. Watersheds in digital spaces: An efficient algorithm based on immersion simulations. *IEEEE Transactions on Pattern Analysis and Machine Intelligence*, 13(6):583–598, June 1991.

[20] E. M. Wescott. Private Communication, 2008.

[21] E. M. Wescott, H. Stenback-Neilsen, M. Conde, Miguel Larsen, and Dirk Lummerzheim. The HEX experiment: Determination of the neutral wind field from 120 to 185 km altitude near a stable premidnight auroral arc by triangulating the drift of rocket-deployed chemical trails. *Journal of Geophysical Research*, 111, 2006.

[22] Tianyu Zhan. *Mesosphere and Lower Thermosphere Neutral Winds Observations Using Rocket-Related Chemical Trails at Poker Flat, Alaska*. PhD thesis, Clemson University, August 2007.